

This thesis is presented for the master's degree of Nagoya University

Estimation of galaxy star formation rate from low radio frequency observations

Shunraro YOSHIDA (ID:261801444)

22 January, 2020

The laboratory of Galaxy Evolution (Ω lab.)
Division of Particle and Astrophysical Science, Graduate School of Science
Nagoya University, Japan

Supervisors: Dr. Tsutomu T. Takeuchi

Dr. Barbara Catinella

Dr. Luca Cortese

Dr. O. Ivy Wong

Abstract

Star formation rate (SFR) is one of the most fundamental quantities of a galaxy. Recombination lines, far-ultraviolet, and infrared (IR) luminosities, for example, are commonly used observational indicators of the SFR (e.g., Kennicutt & Evans 2012). In addition, some references (e.g., Condon 1992) have suggested the use of low-frequency emission (at GHz or lower) as a possibly better-performing SFR indicator compared to the traditional indicators, since it is insensitive to dust extinction. Such an indicator is desirable for deepening the understanding of galaxy evolution because the effect of dust might be the biggest source of uncertainty for the SFR estimation at high- z . However, we still do not understand the galaxy spectral energy distribution at low frequencies due to the lack of observational data up to now. Low-frequency emission is often approximated as a power-law, and recent spatially resolved radio observations show that the spectral index shows a large variety depending on the location in a galaxy (Kapińska et al., 2017; For et al., 2018). This suggests that the radio emission from star-forming galaxies may not have a simple frequency dependence. Therefore, we must investigate how the relation between radio emission and star-formation (SF) activity varies across the low frequencies. In this study, we investigate the frequency dependence of the global low-frequency radio and IR luminosity relation, as measures of SF activity in nearby star-forming galaxies. We select galaxies from the Herschel Reference Survey (HRS) catalog (Boselli et al., 2010), which is assumed to be representative of local galaxies. We identify 18 star-forming galaxies with high-quality radio data from the GaLactic Extragalactic All-sky MWA (GLEAM) survey catalog (Hurley-Walker et al., 2017). The radio sources compiled by the catalog have 20 narrow bands at 72–231 MHz, which allows for a more accurate examination of the frequency dependence. Firstly, we find that a single power-law fitting is valid for modeling the relation of radio with IR luminosities from MWA frequencies to 1.5 GHz. The result suggests that the variation of the spectral index on the local spatial scales do not affect the global relation significantly. Secondly, we find that SFR calculated from the low-frequency radio emission is consistent with SFRs obtained from IR luminosities. We calculated the SFR in two ways: 1) use the fitting result of each galaxy as the calibration for the indicator, and 2) use the averaged quantities for calibration from all sampled galaxies. While the former method gives us more consistent results with a scatter of $\sim 20\%$, the latter results in two times more scatter than the former. Larger scatter in the latter method would be attributed to the intrinsic uncertainty of the calibration. In conclusion, we propose to use the individual spectral energy distribution for calculating the radio SFR with less uncertainty. This study provides a powerful tool for future radio surveys, like the Square Kilometre Array (SKA).

Acknowledgments

I would like to thank Dr. Luca Cortese, Dr. O. Ivy Wong, and Dr. Barbara Catinella for their extraordinary support in my master's research. When I started this research in Australia in August 2018, every single step was new and hard for me. I did not know many things about basic galaxy properties, radio astronomy, and even how to make progress in the research. However, every time I faced a problem, they spared so much time and gave me help and advice. I am grateful for their kindness, and I think my research project can't reach the level without their help. I also thank all of my friends I met in the International Centre for Radio Astronomy Research (ICRAR), Australia. They were always kind to me and gave me much help when I had a problem to do research and to live in a foreign country. During my stay there in a total of about five months, I discussed various fields of astrophysics and also the general topics with them. This experience broadens my horizons and makes my two years master's course much more fruitful than I expected.

I also would like to thank Dr. Tsutomu T. Takeuchi, who is my supervisor at Nagoya University. He gave me so many opportunities to go the outside university and to get extensive knowledge not only in astronomy. He was thoughtful and gave me shrewd advice every time I got stuck on a problem. His admired expertise in astrophysics, statistics, linguistics expands my perspectives. I am grateful for everything he has done for me.

I would like to thank my colleagues and friends in Nagoya University and Osaka University also. They always supported me when I was suffering from the research and my life. I also appreciate my parents to raise me with so much money and time.

This project would have been impossible without funding from Nagoya University (Overseas Challenge Program for Young Researchers 2019).

Contents

Contents	v
List of Figures	vii
List of Tables	ix
1 Introduction	1
1.1 Star Formation Rate (SFR)	1
1.2 Cosmic Star Formation History	3
1.3 Low radio frequencies and SFR	4
2 Theoretical Background	9
2.1 Free-free radiation	9
2.2 Synchrotron radiation	17
2.2.1 Synchrotron Spectra of Optically Thin Radio Sources	22
2.2.2 Synchrotron Self-Absorption	24
3 Data	29
3.1 Herschel Reference Survey (HRS)	29
3.2 GLEAM survey	32
4 Methods	35
4.1 Cross Matching	35
4.2 Reduce galaxy samples for the reliable analysis	36
4.3 Calculating the q_ν parameter	38
4.4 Total IR luminosity	38
4.5 Fitting to q_ν parameters	39
4.6 Calculating the SFR	40

CONTENTS

5 Results	41
5.1 Distributions of γ	41
5.2 Comparing SFR indicators	43
6 Discussions	47
6.1 Comparing the calibration with previous results	47
6.2 Radio SFR uncertainty	49
6.3 Galaxy properties for the radio SFR	50
6.4 Non-detected galaxies by the GLEAM survey	53
7 Summary and Future prospects	55
Bibliography	57
Appendix A Galaxy images	61
A.1 Matched samples (18 samples used for the analysis)	61
A.2 Matched samples (not used for the analysis)	61
A.3 Suspicious matching samples	61
A.4 Not matching samples	61
Appendix B Galaxy samples for the analysis	69
Appendix C Fitting results	71

List of Figures

1.1	Reprint from Madau & Dickinson (2014) (Figure 9)	4
1.2	Adapted from Helou et al. (1985) (Figure 2)	5
1.3	Adapted from Kapińska et al. (2017) (Figure 5)	7
1.4	Adapted from For et al. (2018) (Figure 6)	8
2.1	Reprint from Condon (1992) (Figure 1)	10
2.2	The schematic image of the interaction of an electron with the ion	11
2.3	The acceleration of an electron by an ion	12
2.4	The schematic picture of the cylindrical shell of electrons	13
2.5	The schematic picture of HII region	15
2.6	The spectrum of free-free radiation	16
2.7	The schematic picture of relativistic aberration	20
2.8	Simple configuration of the synchrotron source and observer	21
2.9	Synchrotron pulse by a single electron	22
2.10	The synchrotron spectrum of a single electron	23
2.11	The spectrum of synchrotron radiation	26
2.12	The spectrum of synchrotron radiation from real sources	27
3.1	Reprint from Boselli et al. 2010 (Figure 1)	31
3.2	Reprint from Boselli et al. 2010 (Figure 2)	32
3.3	Reprint from Hurley-Walker et al. 2017 (Figure 11)	33
4.1	Separation from the cross-matching	37
4.2	The comparison of total IR luminosities	39
5.1	Histograms of γ from the fitting	41
5.2	The comparison of γ from different fitting methods	42
5.3	The consistency of the radio SFR	44
5.4	The consistency of the radio SFR with SFR_{IR} and $\text{SFR}_{\text{FUV+24mic}}$	45

LIST OF FIGURES

6.1	Adapted from Calistro Rivera et al. (2017)	48
6.2	Adapted from Chyžý et al. (2018)	49
6.3	Histograms of γ from the fitting (labeled)	51
6.4	q_ν plots for each galaxy with labels	52
A.1	Galaxy images (6/18 used for the analysis)	62
A.2	Galaxy images (12/18 used for the analysis)	63
A.3	Galaxy images (9/15 not used for the analysis)	64
A.4	Galaxy images (6/15 not used for the analysis)	65
A.5	Galaxy images (suspicious matching)	66
A.6	Galaxy images (no matching)	67
C.1	Fitting results for 18 samples (1)	72
C.2	Fitting results for 18 samples (2)	73
C.3	Fitting results for 18 samples (3)	74
C.4	Fitting results for 18 samples (4)	75
C.5	Fitting results for 18 samples (5)	76
C.6	Fitting results for 18 samples (6)	77
C.7	Fitting results for 18 samples (7)	78

List of Tables

B.1 The overview of 18 samples used for the analysis	70
--	----

Chapter 1

Introduction

In this chapter, I introduce three fundamental topics in astrophysics related to our study. In Section 1.1, I mention the importance of studying star formation activity in galaxies and the primary method to measure it. In Section 1.2, I introduce the idea of the cosmic star formation density and the previous result. In Section 1.3, I explain why the low-frequency emission is important for measuring SFR. Here, I also mention the IR-Radio correlation, which is one of the most critical relations in galactic radio astronomy.

1.1 Star Formation Rate (SFR)

Star formation in galaxies is one of the most complex processes. In modern astronomy, understanding it and its evolution is still a challenging problem. To explain these, we need an advanced knowledge of dark matter and baryon physics. The evolution of dark matter is now interpreted by the “ Λ CDM (Cold Dark Matter) model”, which indicates structures in the universe have been forming hierarchically (bottom-up) (e.g., Peebles 1982). This model explains that a galaxy forms in a small dark halo once and merges into other halos to form larger systems as time goes on (Blumenthal et al. 1984). With the advance of computational methods, a cosmological simulation can model this scenario and reproduce structures in the universe (e.g., Navarro & Steinmetz 2000; Vale & Ostriker 2004). However, the baryon evolution inside dark halos is much more difficult to understand because its evolution attributes to the composition of the different scale of physics. Revealing these physics needs as a first step to find constraints by measuring the star formation activity accurately. When we measure the star formation activity at each era in the uni-

CHAPTER 1. INTRODUCTION

verse, we can constrain the galaxy evolution scenario observationally (Section 1.2). The star formation rate (SFR) is the total mass of stars formed in a galaxy per year, and it is typically used for representing the star formation activity in a galaxy. SFR is one of the most fundamental and essential values for understanding galaxy properties and its evolution.

Here, we present the SFR calibration methods. The fundamental equation to calculate SFR at time t from intrinsic stellar luminosity at the wavelength of λ is shown below (Buat 1991):

$$L(\lambda, t) = \int_0^t \int_{M_{\text{low}}}^{M_{\text{up}}} F_\lambda(m, \theta) \text{SFR}(t - \theta) \psi(m) dm d\theta \quad (1.1)$$

where $F_\lambda(m, \theta)$ is the stellar evolutionary tracks, $\psi(m)$ is the Initial Mass Function (IMF; e.g., Chabrier 2003; Kroupa 2001; Salpeter 1955) and M_{up} (M_{low}) is the upper (lower) limit of the stellar mass considered for the calculation.

Indeed, we can calculate SFR from Equation 1.1 in two ways. One way is to assume a specific stellar synthesis model and star formation history and to estimate parameters to reproduce luminosities, which we can observe at present. This method is called SED fitting, and it is useful even for the galaxies experienced not stable star formation recently. However, this method highly depends on the star formation history chosen for the calculation.

Another way is to assume that SFR is constant over a specific timescale T , and SFR is proportional to the luminosity. Although the timescale T depends on the wavelength for measuring, it is simple to calculate SFR with a specific luminosity. In this case, we can measure SFR with the following equation:

$$\text{SFR} = C \times L(\lambda) \quad (1.2)$$

where C is a constant.

This method is relatively easy to measure SFR from observation, but the assumption of a constant SFR is sometimes problematic. Previous research shows the required time to reach the steady-state is \sim Myr for hydrogen recombination lines (e.g., H α ; $\lambda = 6563 \text{ \AA}$, H β ; $\lambda = 4861 \text{ \AA}$), ~ 100 Myr for the Far-ultraviolet (FUV) to IR emissions (Hao et al. 2011; Kennicutt & Evans 2012; Murphy et al. 2011). These results show that the SFR calculated from Equation 1.2 is different from the actual value if SFR varies among ~ 10 Myr (e.g., intense starburst).

Considering this problem, hydrogen recombination lines emitted by the young (\leq

10^7 yr) and massive ($M > 10 M_{\odot}$) OB stars are more reliable SFR indicators. However, in these cases, we should correct the dust extinction with the Balmer decrement, which is the ratio between H α and H β fluxes (Lequeux et al. 1981), or with IR luminosities (Kennicutt et al. 2009). In addition to this, we need to eliminate [NII] line contamination ($\lambda = 6548 \text{ \AA}, 6584 \text{ \AA}$) from H α emission, and correct the absorption of H β by the young stellar atmosphere. Although recombination lines are good SFR indicators in terms of the time scale in a constant star formation, the calibration for them gives us non-negligible uncertainty.

FUV emission is emitted by the AB stars and it is reliable as SFR indicator if the star formation timescale can be assumed more than 10^8 yr. Because of its wavelength (*GALEX* FUV; 1516 \AA), we need to correct the dust extinction also for FUV. We often use IR luminosities for the dust correction based on the idea that dust grains absorbing FUV light re-emits it at a wavelength range of IR (Kennicutt 1998; Murphy et al. 2011). The combination of FUV and IR emissions for estimating SFR is one of the most popular SFR indicators (e.g., FUV + 24mic, FUV + total IR).

Besides these indicators, in this study, we focus on the low-frequency radio emission around ~ 100 MHz because it is also an SFR indicator guaranteed by its correlated with (Far) IR emissions and SFR in galaxies (Section 1.3).

1.2 Cosmic Star Formation History

Tinsley & Danly (1980) proposed the cosmic star formation history, which shows the SFR density evolution in the universe. While no one could observe much more high- z galaxies enough to do the statistics at that time, we can now observe intrinsic FUV and IR luminosities from a large number of galaxies up to $z \sim 4$ (and up to $z \sim 7$ with only ultraviolet). Recent studies (Hopkins & Beacom 2006; Madau & Dickinson 2014) make a cosmic star formation history with a consistent IMF over all the redshift range. Their plots represent that the peak of the star formation happened at $z \sim 1.9$, where 3.5 Gyr after the Big Bang (Figure 1.1). The era when the SFR density was the highest is called “Cosmic Noon” because the star formation in the universe was the most active. The period before Cosmic Noon ($z > 1.9$) is called “Cosmic dawn”.

Although now we know the cosmic star formation history up to $z \sim 8$ ($z > 4$ is still ambiguous due to the lack of IR observation), extending it to the earlier universe is quite difficult because we do not have a telescope to observe IR luminosity from high- z galaxies with a large field of view. FUV emission from high- z galaxies also has difficulty for the

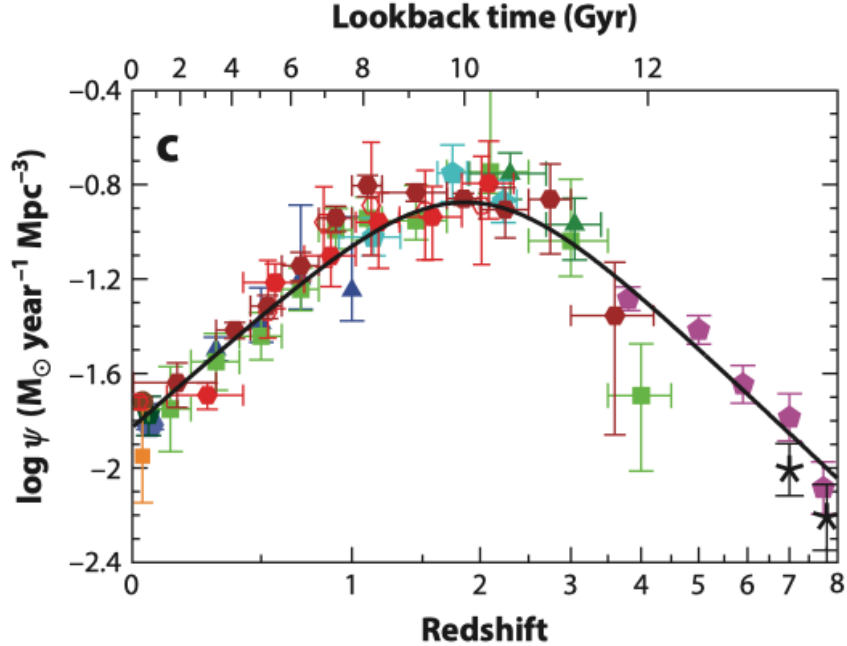


Figure 1.1: (Reprint from Madau & Dickinson (2014), Figure 9)

This figure shows the cosmic star formation history from UV and IR emissions. For calculating SFR, they adopt Salpeter IMF. The black solid line shows the best fitting line. We can see the peak of SFR density in the universe at $z \sim 1.9$

calibration because the dust correction for high- z galaxies still has significant uncertainty.

On the contrary, the low-frequency emission is an extinction-free estimator, and we will be able to observe high- z galaxies with high sensitivity and large field of view enough to extend the cosmic star formation history.

1.3 Low radio frequencies and SFR

The low-frequency radio emission from star-forming galaxies has been studied for many years. In this paper, we use the term “Low frequency” as the frequency of a few GHz and less than that. At this frequency range, synchrotron emission is supposed to be dominant in star-forming galaxies (Condon 1992). The importance of this emission increased after the global log-linear correlation with infrared (IR) had been found. This correlation was discovered by Helou et al. (1985) using integrated far-infrared (FIR; 60 μm and 100 μm) and 1.4 GHz radio luminosities in star-forming galaxies (Figure 1.2). Hereafter, we use the term “IR-Radio Correlation (IRC)”, although this correlation is originally called FIR-Radio Correlation. This is because we tend to examine the correlation of radio with the total IR luminosity instead of FIR after Bell (2003).

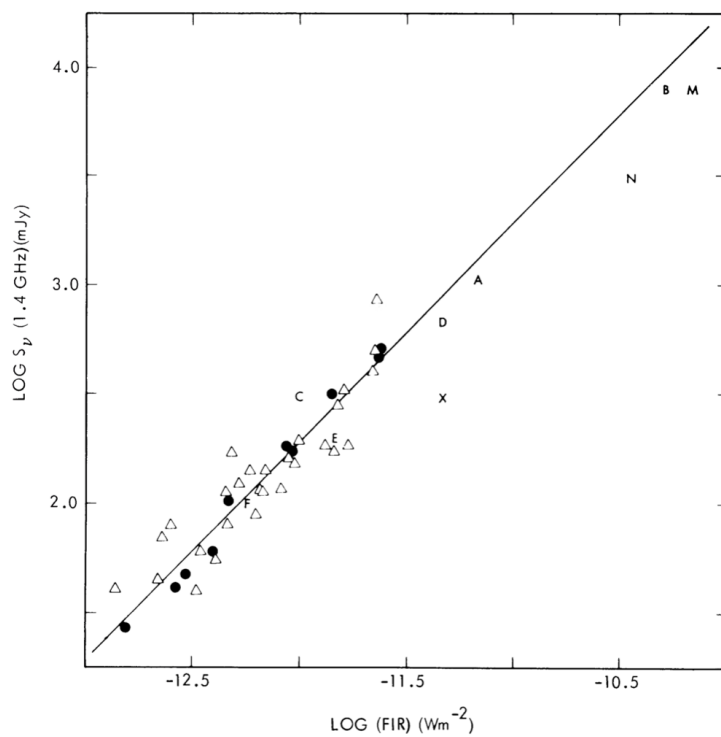


Figure 1.2: (Adapted from Helou et al. (1985), Figure 2)

This figure shows the comparison between FIR and radio at 1.4 GHz fluxes for each galaxy. We can see the tight correlation between them.

CHAPTER 1. INTRODUCTION

Bell (2003); Condon et al. (1991); Yun et al. (2001) have examined this global correlation using a different sample set and found it holds the tightness across more than three orders of magnitude. Recently, the low-frequency survey at around 100 MHz was operated by the LOw Frequency Array (LOFAR; van Haarlem et al. 2013) and the Murchison Widefield Array (MWA; Tingay et al. 2013). With the advent of these telescopes, Calistro Rivera et al. (2017); Read et al. (2018); Wang et al. (2019) extend the study to at an order of magnitude lower frequency and find the correlation is held at not only 1.4 GHz but also ~ 100 MHz. Thanks to this correlation, we can regard the low-frequency emission as an SFR indicator. Synchrotron emission is supposed to be dominant at low frequencies is emitted by the high-energy electrons accelerated by supernova remnants with the magnetic field in a galaxy, and it should trace the star formation activity in star-forming galaxies. To explain IRC physically, Völk (1989) proposed “the calorimeter model”. This model says that all energies from high energy electrons consumed before escaping from galaxies are linearly correlated with all energies re-radiated as IR emissions by dust absorbing all FUV emission from young stars. If this model is valid, IRC has a slope of unity. However, recent studies show that the slope is not unity, and the calorimeter model is not always accurate (Calistro Rivera et al. 2017; Read et al. 2018). Since the low-frequency emission is not affected by the dust extinction (Murphy et al. 2011; Yun et al. 2001), and it will be observed from distant galaxies by the future extended survey, we anticipate its usefulness. We need a further investigation of the relation between the radio and IR luminosities, especially its frequency dependence.

However, the spatially-resolved studies show that a star-forming galaxy emits the radio emission whose spectral index depends on the galaxy region (For et al. 2018; Heesen et al. 2019; Kapińska et al. 2017) (Figure 1.3 and 1.4). This result means that the radio emission is sensitive to the local density environment of the ISM, and it is not guaranteed a simple frequency dependence of the global relation between the integrated radio and IR luminosities.

The integrated radio emission in star-forming galaxies across 100 MHz to 1.4 GHz is supposed to compose of a few percents to 10% free-free and the synchrotron radiations (Condon 1992). Each radiation is emitted by electrons interacted with the electric field of ions in the HII region or the magnetic field in a galaxy (Chapter 2). For emitting the synchrotron radiation, an electron needs to be accelerated to the light speed by the supernova remnant. While the synchrotron emission is expected to be dominant at these low frequencies, previous studies find the sign of the free-free absorption and flatter or turnover spectral (Chyžík et al. 2018; Schober et al. 2017). If the radio emission has a significant turnover among low frequencies, global IRC does not have a simple frequency

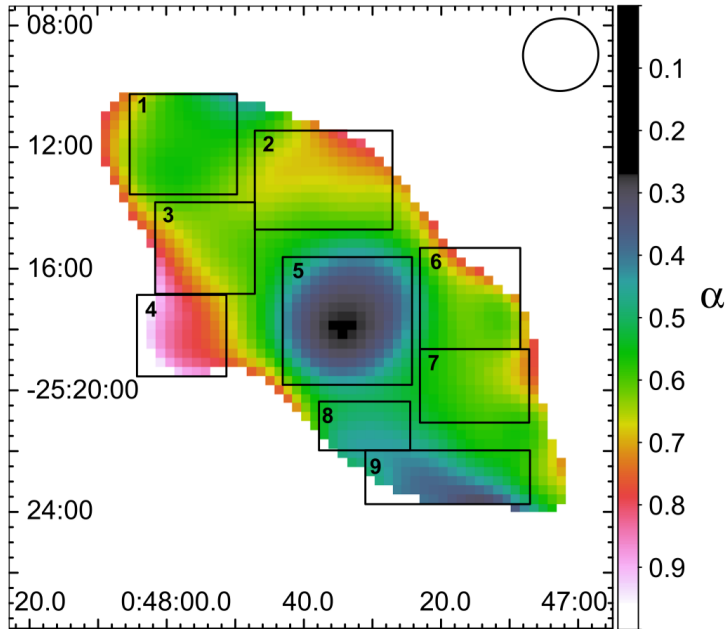


Figure 1.3: (Adapted from Kapińska et al. (2017), Figure 5)

This figure shows the distribution of the radio spectral index in NGC 253. They do the fitting between 200 MHz (GLEAM; Hurley-Walker et al. 2017) and 1.465 GHz (Carilli et al. 1992). The color scale is for the spectral index and the pixel size is $18 \times 18 \text{ arcsec}^2$.

dependence, and the radio emission is no longer useful as an SFR indicator.

In this study, we investigate nearby star-forming galaxies from the reference sample for ensuring the reliability of measuring the SFR from the low-frequency emission. For examining the general trend, we use star-forming galaxy samples from the Herschel Reference Survey (HRS; Boselli et al. 2010) catalog and the low-frequency emission from The Galactic Extragalactic All-sky MWA (GLEAM; Hurley-Walker et al. 2017) survey. The HRS catalog is supposed to represent the local galaxy samples (Section 3.1). The GLEAM survey observes the mJy scale radio emission from large areas with their 20 narrow bands (Section 3.2).

This paper is organized as follows. In Chapter 3, I introduce our galaxy samples and the low-frequency emissions used in this study. In Chapter 4, I mention the way to investigate its frequency dependence and derive the radio SFR. In Chapter 5, I show our results about the frequency dependence of IRC and the consistency of the radio SFR. In Chapter 6, I compare our results with previous studies. Finally, we summarize our study in Chapter 7.

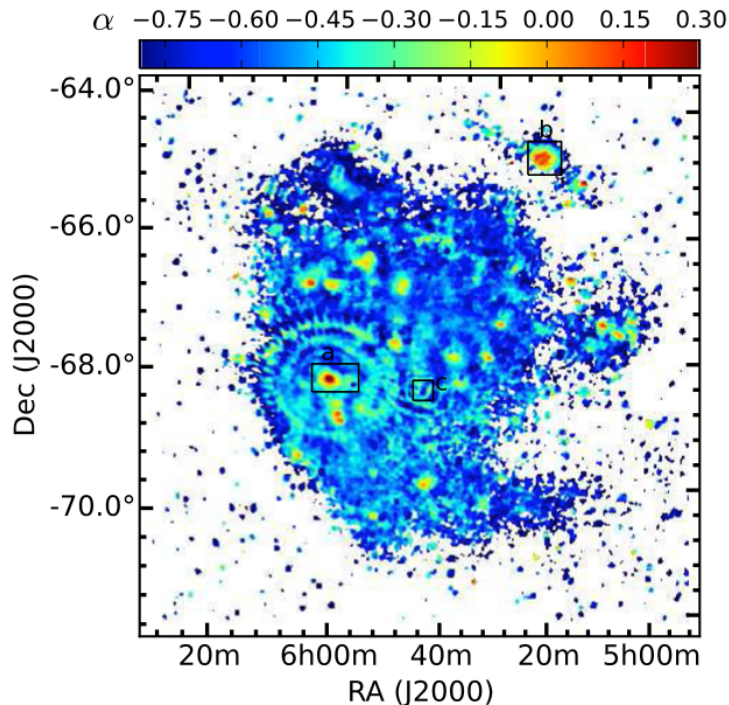


Figure 1.4: (Adapted from For et al. (2018), Figure 6)

This figure shows the distribution of the radio spectral index in Large Magellanic Could (LMC). They do the fitting between 166 MHz (GLEAM; Hurley-Walker et al. 2017) and 1.4 GHz (Hughes et al. 2007). The color scale is for the spectral index and the pixel size is $34.9 \times 34.9 \text{ arcsec}^2$ at GLEAM 166MHz.

Chapter 2

Theoretical Background

In this chapter, I describe physical mechanisms of radio emissions related to our study. At low frequencies, we observe free-free¹ (Bremsstrahlung) and synchrotron² radiations. Both emissions are the continuum emission. While the free-free radiation is usually dominant from a galaxy at $30 \sim 200$ GHz, the synchrotron radiation is dominant less than 30 GHz (Figure 2.1).

2.1 Free-free radiation

The free electrons produce free-free radiation by scattering off ions. In star-forming galaxies, the radiation source of this emission is the HII region where young massive (OB) stars ionized most of the hydrogen atoms. In this section, we consider the radiation mechanism of free-free radiation. Here, we consider only electrons emit the radiation because an electron is much more accelerated than an ion due to the difference of their mass (an electron is 1840 times lighter than a proton).

Firstly, I consider the simplest case that a single electron passes by the ion and emits the radiation. Note that the path of the electron does not change after the interaction because the energy of radio emission is much smaller than the mean electron energy in a plasma.

¹<https://www.cv.nrao.edu/~sransom/web/Ch4.html>

²<https://www.cv.nrao.edu/~sransom/web/Ch5.html>

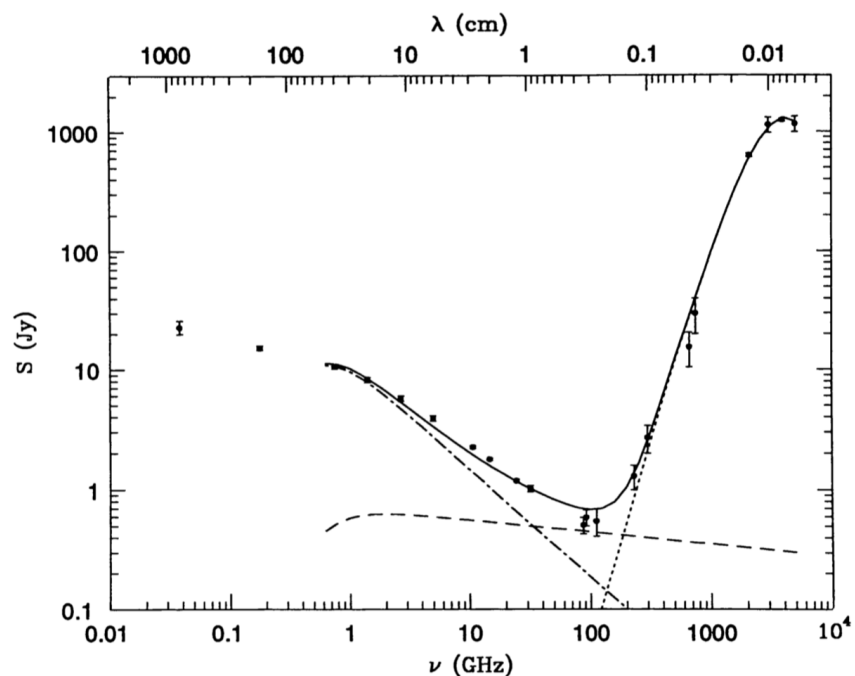


Figure 2.1: (Reprint from Condon (1992), Figure 1)

This figure shows the spectral energy distribution of M82. The dotted line shows the dust thermal emission which is dominant at higher than 200 GHz. The dashed line shows the free-free radiation from the HII regions around massive stars, which is dominant at 30 \sim 200 GHz. The dot-dash line shows the synchrotron radiation emitted by the high energy electrons, which is dominant at less than 30 GHz.

$$\frac{E_{10\text{ GHz}}}{\langle E_e \rangle} = \frac{h \times 10^{10} \text{ Hz}}{3kT/2} = \frac{6.63 \times 10^{-27} \text{ erg s} \times 10^{10} \text{ Hz}}{1.5 \cdot 1.38 \times 10^{-16} \text{ erg K}^{-1} \cdot 10^4 \text{ K}} = 3.3 \times 10^{-5} \quad (2.1)$$

During the interaction, the electron is accelerated by the electric field by the ion. Then, we can write the equation of motion for parallel and perpendicular to the electron's path (Figure 2.2):

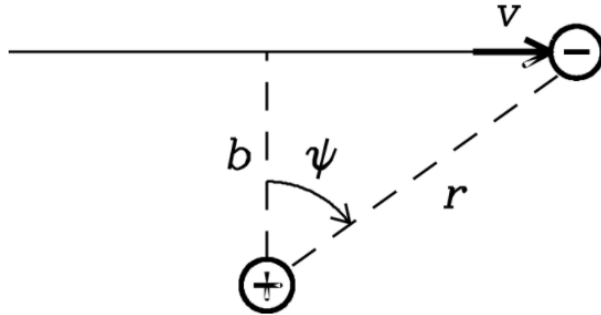


Figure 2.2: This figure shows the schematic picture of the interaction of an electron with the ion. b and $\tau = b/v$ are called the impact parameter and the collision time, respectively.

$$F_{\parallel} = m_e \dot{v}_{\parallel} = \frac{-Ze^2}{r^2} \sin \psi = \frac{-Ze^2 \sin \psi \cos^2 \psi}{b^2} \quad (2.2)$$

$$F_{\perp} = m_e \dot{v}_{\perp} = \frac{Ze^2}{r^2} \cos \psi = \frac{Ze^2 \cos^3 \psi}{b^2} \quad (2.3)$$

where b is the impact parameter and $\cos \psi = \frac{b}{r}$.

These accelerations show different shapes of the pulse (Figure 2.3). Since the parallel acceleration produces some infrared radiation with the angular frequency $\omega \sim \tau^{-1} = \frac{v}{b}$ (τ is a collision time), its contribution is negligible at radio frequency.

Therefore, the power of free-free radiation from the acceleration of the electron perpendicular to its velocity is:

$$P = \frac{2}{3} \frac{e^2 \dot{v}_{\perp}^2}{c^3} = \frac{2e^2 Z^2 e^4}{3c^3 m_e^2} \left(\frac{\cos^3 \psi}{b^2} \right)^2 \quad (2.4)$$

where we insert \dot{v}_{\perp} into the Larmor's formula $(P = \frac{2}{3} \frac{q^2 \dot{v}^2}{c^3}, q \text{ is a charge})$, which shows the power emitted by the accelerated particles.

We can get the total energy of W by the pulse as follows:

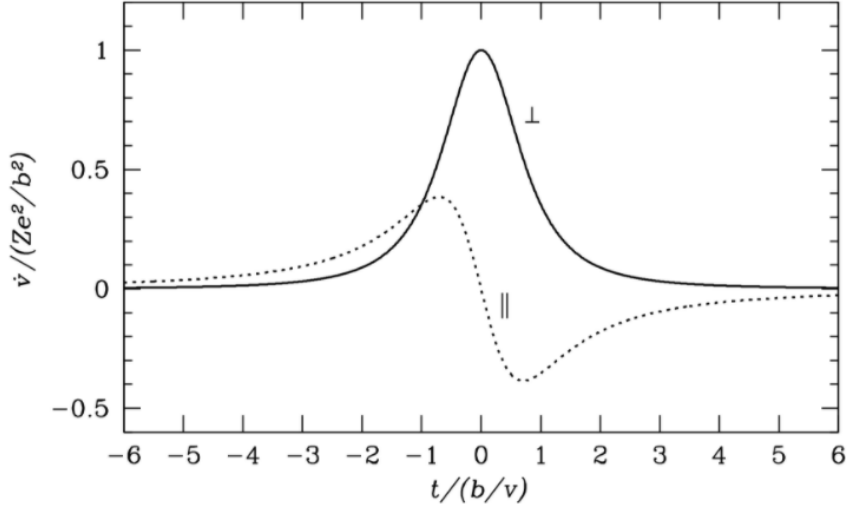


Figure 2.3: This figure shows the acceleration of an electron. The solid and dotted lines show the case of perpendicular and parallel to the electron's velocity, respectively.

$$W = \int_{-\infty}^{\infty} P dt \quad (2.5)$$

As I noted above, the electrons' velocity is constant so that we can change of variables:

$$v = \frac{dx}{dt} \quad \text{and} \quad \tan \psi = \frac{x}{b} \quad (2.6)$$

then,

$$v = \frac{b d(\tan \psi)}{dt} = \frac{b \sec^2 \psi d\psi}{dt} = \frac{b d\psi}{\cos^2 \psi dt} \quad (2.7)$$

and

$$dt = \frac{b}{v \cos^2 \psi} d\psi \quad (2.8)$$

Substituting Equation 2.4 and 2.8 into Equation 2.5 yields

$$W = \frac{2}{3} \frac{Z^2 e^6}{c^3 m_e^2 b^4} \int_{-\pi/2}^{\pi/2} \frac{b \cos^6 \psi}{v \cos^2 \psi} d\psi = \frac{4}{3} \frac{Z^2 e^6}{c^3 m_e^2 b^3 v} \int_0^{\pi/2} \cos^4 \psi d\psi = \frac{\pi Z^2 e^6}{4 c^3 m_e^2} \left(\frac{1}{b^3 v} \right) \quad (2.9)$$

where $\int_0^{\pi/2} \cos^4 \psi d\psi = \frac{3\pi}{16}$.

The pulse energy W shows the total energy emitted by a single electron interaction characterized by the impact parameter b and the electron's velocity v .

Secondly, I consider the strength and spectral of free-free radiation from HII region with several simple assumptions. Here, I assume the local thermodynamic equilibrium (LTE) in the HII region. In LTE, electrons have a much higher speed than ions because of the difference of their mass, although the average kinetic energy of electrons and ions are equal. Therefore, we can think ions do not move by the interactions.

When I consider the cylindrical shell around the ion (Figure 2.4), I can calculate the number of electrons passing any ion per unit time between b and $b + db$ under the velocity range of dv :

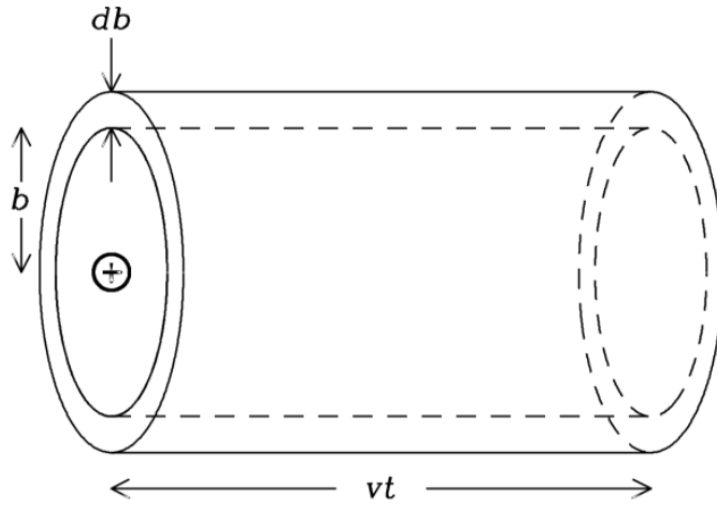


Figure 2.4: This figure shows the schematic picture that an electron passes the ion in the cylindrical shell.

$$n_e (2\pi b, db) v f(v) dv \quad (2.10)$$

where $f(v)$ is the normalized speed distribution of electrons (In LTE, $f(v)$ is the Maxwellian distribution).

The number $\dot{n}_c(v, b)$ of such collisions per unit volume per unit time is:

$$\dot{n}_c(v, b) = (2\pi b) v f(v) n_e n_i \quad (2.11)$$

Then, I can write the emission coefficient j_ν as follows:

$$4\pi j_\nu = \int_{b=0}^{\infty} \int_{v=0}^{\infty} W_\nu(v, b) \dot{n}_c(v, b) dv db \quad (2.12)$$

where $W_\nu(v, b)$ is the average energy per unit frequency emitted during a single interaction

CHAPTER 2. THEORETICAL BACKGROUND

and approximately written in $W_\nu(v, b) = \frac{W}{\nu_{\max}(=v/2\pi b)}$.

Substituting $W_\nu(v, b)$ and Equation 2.11 into Equation 2.12 yields

$$4\pi j_\nu = \int_{b=0}^{\infty} \int_{v=0}^{\infty} \left(\frac{\pi^2 Z^2 e^6}{2c^3 m_e^2 b^2 v^2} \right) 2\pi b db n_e n_i v f(v) dv \quad (2.13)$$

$$= \frac{\pi^3 Z^2 e^6 n_e n_i}{c^3 m_e^2} \left(\frac{2m_e}{\pi k T} \right)^{1/2} \int_{b=0}^{\infty} \frac{db}{b} \quad (2.14)$$

where I use the Maxwellian distribution:

$$f(v) = \frac{4v^2}{\sqrt{\pi}} \left(\frac{m_e}{2kT} \right)^{3/2} \exp \left(-\frac{m_e v^2}{2kT} \right) \quad (2.15)$$

Note that $\int_{b=0}^{\infty} \frac{db}{b}$ diverges, so it needs finite limites b_{\min} and b_{\max} . To estimate v_{\min} , let's consider the change in momentum during the single electron-ion interaction:

$$m_e \Delta v = \int_{-\infty}^{\infty} F dt = \int_{-\infty}^{\infty} \left(\frac{Ze^2 \cos \psi}{r^2} \right) dt = Ze^2 \int_{-\infty}^{\infty} \frac{\cos^3 \psi}{b^2} dt \quad (2.16)$$

$$= \frac{Ze^2}{bv} \int_{-\pi/2}^{\pi/2} \cos \psi d\psi = \frac{2Ze^2}{bv} \quad (2.17)$$

$$= \frac{2Ze^2}{bv} (< 2m_e v) \quad (2.18)$$

where the maximum momentum transfer $m_e \Delta v$ is twice the initial momentum m_v .

Therefore, the minimum impact parameter b_{\min} is

$$b_{\min} = \frac{Ze^2}{m_e v^2} \quad (2.19)$$

To estimate the maximum impact parameter b_{\max} , let's consider ν_{\max} and get $b_{\max} = \frac{v}{2\pi\nu}$ because the pulse power is not significant at frequency ν above b_{\max} . In some textbooks, they consider b_{\max} with the Debye length, which shows the characteristic scale of the electric shielding. However, this length scale is much larger than b_{\max} obtained here, and it is inappropriate for the calculation in the typical HII region.

These limits (b_{\min}, b_{\max}) yield

$$\frac{b_{\max}}{b_{\min}} \sim \left(\frac{3kT}{m_e} \right)^{1/2} (2\pi\nu)^{-1} \left(\frac{3kT}{Ze^2} \right) \sim \left(\frac{3kT}{m_e} \right)^{3/2} \frac{m_e}{2\pi Ze^2 \nu} \sim 10^5 \quad (2.20)$$

However, this value varies logarithmically in Equation 2.14, and it has small uncer-

tainty. Therefore, these limits have little effect on the calculation.

Since the HII region is in LTE, it is possible to consider Kirchhoff's law and absorption coefficient κ in the Rayleigh-Jeans limit:

$$\kappa = \frac{j_\nu}{B_\nu(T)} \sim \frac{j_\nu c^2}{2kT\nu^2} = \frac{1}{\nu^2 T^{3/2}} \left[\frac{Z^2 e^6}{c} n_e n_i \frac{1}{\sqrt{2\pi (m_e k)^3}} \right] \frac{\pi^2}{4} \ln \left(\frac{b_{\max}}{b_{\min}} \right) \quad (2.21)$$

where $B_\nu(T)$ is the blackbody brightness.

The absorption coefficient κ is proportional to ν^{-2} (To be precise, it is proportional to $\nu^{-2.1}$ due to the frequency dependence of b_{\max}).

Now I can calculate the total opacity τ of HII region if I assume the simple cylindrical shape with a uniform density for the HII region (Figure 2.5)

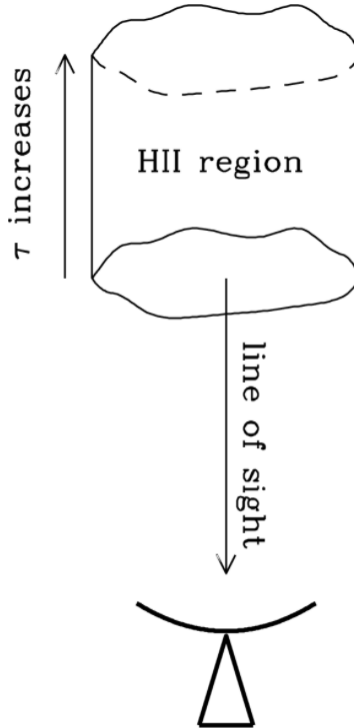


Figure 2.5: This figure shows the schematic picture of the HII region. Astronomers often approximate HII regions by the uniform cylinders. Cylindrical assumption lets us to calculate optical depth τ easily.

$$\tau = - \int_{\text{los}} \kappa ds \propto \int \frac{n_e n_i}{\nu^{2.1} T^{3/2}} ds \sim \int \frac{n_e^2}{\nu^{2.1} T^{3/2}} ds \quad (2.22)$$

where s is the depth of HII region parallel to the line of sight.

CHAPTER 2. THEORETICAL BACKGROUND

At low frequencies enough that $\tau \gg 1$, the HII region becomes opaque, and the spectrum approaches the blackbody. In this case, the brightness temperature approaches the electron temperature ($T \sim 10^4$ K) and its flux density S is in the Rayleigh-Jeans limit ($S \propto \nu^2$). On the other hand, at frequency $\tau \ll 1$, the HII region is transparent and $S \propto \frac{2kT\nu^2}{c^2}\tau(\nu) \propto \nu^{-0.1}$.

I show the spectrum of free-free radiation of the HII region in Figure 2.6.

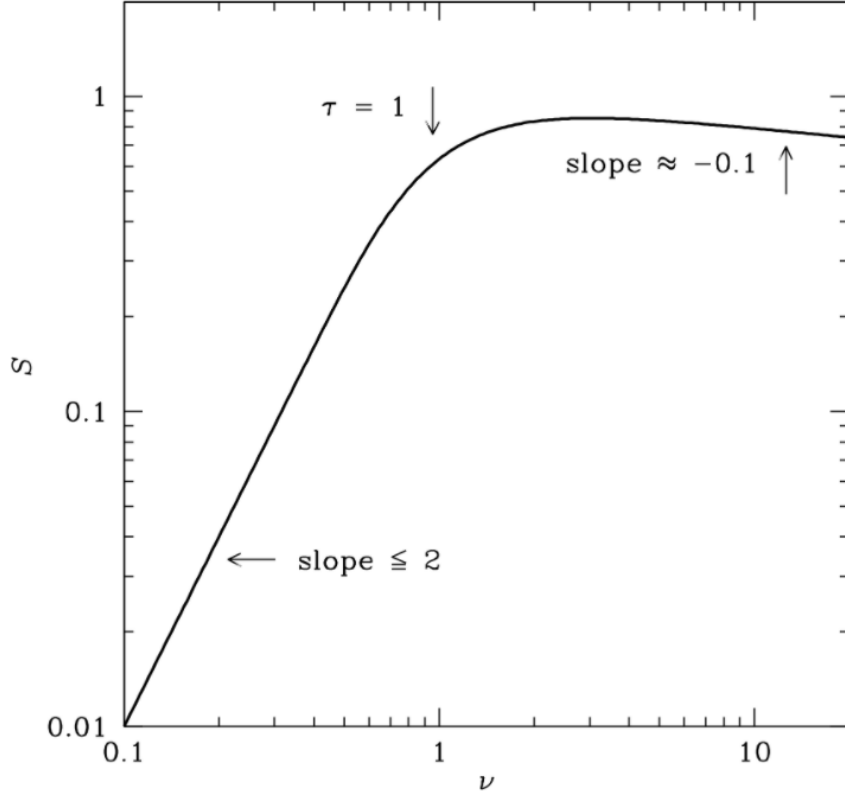


Figure 2.6: This figure shows the radio spectrum of free-free emission. At low frequencies, we can see the blackbody with the slope ≤ 2 . The assumption of the uniform cylinder gives the slope 2, but the non-uniform HII region emits free-free radiation with the slope less than 2. At frequencies higher than the frequency of $\tau = 1$, the slope is nearly flat (-0.1).

At low frequencies, the spectral index α on the log-log plot is useful to describe the radiation mechanism. The definition of α is below:

$$\alpha \equiv \pm \frac{d \log S}{d \log \nu} \quad (2.23)$$

where the sign depends on the literature.

With the + sign convention, the spectral index of HII region well above the break frequency ($\tau = 1$) is $\alpha = -0.1$.

Finally, I mention the idea of emission measure (EM) often used for understanding the physical condition in the HII region. The definition of EM is

$$\frac{\text{EM}}{\text{pc} \cdot \text{cm}^{-6}} \equiv \int_{\text{los}} \left(\frac{n_e}{\text{cm}^{-3}} \right)^2 \text{d} \left(\frac{s}{\text{pc}} \right) \quad (2.24)$$

Then, we can write the optical depth τ in

$$\tau \sim 3.014 \times 10^{-2} \left(\frac{T}{\text{K}} \right)^{-3/2} \left(\frac{\nu}{\text{GHz}} \right)^{-2} \left(\frac{\text{EM}}{\text{pc} \cdot \text{cm}^{-6}} \right) brag_{\text{ff}} \quad (2.25)$$

where $\langle g_{\text{ff}} \rangle$ is the free-free Gaunt factor:

$$\langle g_{\text{ff}} \rangle \sim \ln \left[4.955 \times 10^{-2} \left(\frac{\nu}{\text{GHz}} \right)^{-1} \right] + 1.5 \ln \left(\frac{T}{\text{K}} \right) \quad (2.26)$$

Mezger & Henderson (1967) found the excellent approximation for the free-free opacity τ is

$$\tau \sim 3.28 \times 10^{-7} \left(\frac{T}{10^4 \text{K}} \right)^{-1.35} \left(\frac{\nu}{\text{GHz}} \right)^{-2.1} \left(\frac{\text{EM}}{\text{pc} \cdot \text{cm}^{-6}} \right) \quad (2.27)$$

When we observe the break frequency ν , then we can calculate EM with the electron temperature ($\sim 10^4$ K). And also, we can calculate the gas density in the HII region if we know its size (depth).

2.2 Synchrotron radiation

Synchrotron radiation is a continuum emission which is usually dominant at less than 30 GHz in star-forming galaxies. The interaction of high energy (relativistic) electrons accelerated by the supernova remnant or the galactic nuclei with the galactic magnetic field causes the radiation. Since high energy electrons have a power-law energy distribution, we usually call the radiation “non-thermal synchrotron radiation”. If electrons have a much smaller velocity than the light, they emit the cyclotron radiation with the cyclotron frequency $\omega = \frac{eB}{m_e c}$ in cgs unit (e is a charge, B is the strength of the magnetic field, m_e is a mass of an electron and c is the speed of light). In the normal star-forming galaxies ($B \sim 10 \mu\text{G}$), the electron gyro frequency is 30 Hz and we cannot observe it because it is much smaller frequency than the plasma frequency.

In this section, I show the mechanism to emit synchrotron radiation. Firstly, I focus

CHAPTER 2. THEORETICAL BACKGROUND

on synchrotron radiation emitted by a single electron. Here, I use primed coordinates for the inertial frame in which an electron is at rest and unprimed coordinates for the frame of an observer at rest. Then, I can write down the radiated power with Larmor's equation in the electron rest frame:

$$P' = \frac{2(e')^2 (a'_\perp)^2}{3c^3} = \frac{2e^2 (a'_\perp)^2}{3c^3} \quad (2.28)$$

where $e' = e$ because the electric charge is a relativistic invariant.

If an electron passes on x -axis in the magnetic field, its acceleration is only y and z -axis because of the Lorentz force. Applying the chain rule to the acceleration by the magnetic field $a_\perp = (a_y^2 + a_z^2)^{1/2}$ in the rest frame of an observer yields

$$a_y \equiv \frac{dv_y}{dt} = \frac{dv_y}{dt'} \frac{dt'}{dt} = \frac{1}{\gamma} \frac{dv'_y}{dt'} \frac{dt'}{dt} = \frac{a'_y}{\gamma^2} \quad \left(a_z \equiv \frac{dv_z}{dt} = \frac{a'_z}{\gamma^2} \right) \quad (2.29)$$

Then,

$$a_\perp = \frac{a'_\perp}{\gamma^2} \quad (2.30)$$

Thus,

$$P' = \frac{2e^2 (a'_\perp)^2}{3c^3} = \frac{2e^2 a_\perp^2 \gamma^4}{3c^3} \quad (2.31)$$

Now, I need to transform $P' = \frac{dE'}{dt'}$ into $P = \frac{dE}{dt}$. The chain rule derives

$$P \equiv \frac{dE}{dt} = \frac{dE}{dt'} \frac{dt'}{dt} = \frac{dE}{dE'} \frac{dE'}{dt'} \frac{dt'}{dt} = \gamma P' \gamma^{-1} = P' \quad (2.32)$$

The radiated power is also the relativistic invariant.

Consequently,

$$P = P' = \frac{2e^2 a_\perp^2 \gamma^4}{3c^3} \quad (a_{||} = 0) \quad (2.33)$$

To calculate a_\perp , $a_\perp = \frac{dv_\perp}{dt} = \omega_B v_\perp$. Since electrons to emit synchrotron radiation are relativistic, the angular frequency ω_B is $\omega_B = \frac{eB}{(\gamma m_e)c}$. Then,

$$a_\perp = \frac{eBv_\perp}{\gamma m_e c} = \frac{eBv \sin \alpha}{\gamma m_e c} \quad (2.34)$$

where α shows the pitch angle between the electron velocity and the magnetic field B .

Inserting Equation 2.34 into Equation 2.33 yields

$$P = \frac{2e^2}{3c^3} \gamma^2 \frac{e^2 B^2}{m_e^2 c^2} v^2 \sin^2 \alpha \quad (2.35)$$

For simplicity, this equation often is written in

$$P = 2\sigma_T \beta^2 \gamma^2 c U_B \sin^2 \alpha \quad (2.36)$$

where σ_T is the Thomson cross-section of an electron, $\beta = \frac{v}{c}$ and U_B is the magnetic energy density ($U_B = \frac{B^2}{8\pi}$).

Therefore, the synchrotron power radiated by a single electron depends on γ , U_B and α ($\beta \sim 1$ if $\gamma \gg 1$)

The relativistic electrons can have lifetimes of thousands to millions of years before losing their energy via synchrotron radiation or other physical processes. During their lifetimes, electrons scattering with the galactic magnetic field and charged particles repeatedly.

In this case, the distribution of the pitch angle α becomes random and isotropic, and we can derive the averaged synchrotron power $\langle P \rangle$ per electron over all possible α :

$$\langle P \rangle = 2\sigma_T \beta^2 \gamma^2 c U_B \langle \sin^2 \alpha \rangle = \frac{4}{3} \sigma_T \beta^2 \gamma^2 c U_B \quad (2.37)$$

where

$$\begin{aligned} \langle \sin^2 \alpha \rangle &\equiv \frac{\int \sin^2 \alpha d\Omega}{\int d\Omega} = \frac{1}{4\pi} \int \sin^2 \alpha d\Omega \\ &= \frac{1}{4\pi} \int \phi = 0^{2\pi} \int_{\alpha=0}^{\pi} \sin^2 \alpha \sin \alpha d\alpha d\phi = \frac{1}{4\pi} 2\pi \frac{4}{3} \\ &= \frac{2}{3} \end{aligned} \quad (2.38)$$

Here I describe the beaming effect, which is the specific feature of synchrotron radiation due to the relativistic electrons. The relation between v_x at the frame of the observer (unprimed) and v'_x at the rest frame of the electron (primed) is

$$\begin{aligned} v_x &\equiv \frac{dx}{dt} = \frac{dx}{dt'} \frac{dt'}{dt} = \gamma \left(\frac{dx'}{dt'} + v \frac{dt'}{dt} \right) \left(\frac{dt}{dt'} \right)^{-1} \\ &= \gamma (v'_x + v) \left[\gamma \left(1 + \frac{\beta}{c} \frac{dx'}{dt'} \right) \right]^{-1} \\ &= (v'_x + v) \left(1 + \frac{\beta v'_x}{c} \right)^{-1} \end{aligned} \quad (2.39)$$

In the y -direction,

CHAPTER 2. THEORETICAL BACKGROUND

$$\begin{aligned} v_y &\equiv \frac{dy}{dt} = \frac{dy}{dt'} \frac{dt'}{dt} = \frac{dy'}{dt'} \left(\frac{dt}{dt'} \right)^{-1} \\ &= \frac{v'_y}{\gamma} \left(1 + \frac{\beta v'_x}{c} \right)^{-1} \end{aligned} \quad (2.40)$$

In the electron's rest frame, if an electron emits synchrotron photons with speed c at an angle θ' from x' -axis, then the relation among θ' , v' and c is

$$\cos \theta' = \frac{v'_x}{c}, \quad \sin \theta' = \frac{v'_y}{c} \quad (2.41)$$

In the observer's rest frame, we can write in the same way:

$$\cos \theta = \frac{v_x}{c}, \quad \sin \theta = \frac{v_y}{c} \quad (2.42)$$

Using Equation 2.39, 2.40, 2.41 and 2.42 to eliminate v and v' yields the relation between θ and θ' :

$$\begin{aligned} \cos \theta &= \left(\frac{v'_x + v}{1 + \beta v'_x/c} \right) \frac{1}{c} = \left(\frac{c \cos \theta' + v}{1 + \beta c \cos \theta'/c} \right) \frac{1}{c} = \frac{\cos \theta' + \beta}{1 + \beta \cos \theta'} \\ \sin \theta &= \frac{v'_y}{c \gamma (1 + \beta v'_x/c)} = \frac{\sin \theta'}{\gamma (1 + \beta \cos \theta')} \end{aligned} \quad (2.43)$$

In the electron's rest frame, Larmor's equation implies a power pattern proportional to $\cos^2 \theta'$ with nulls at $\theta' = \pm \frac{\pi}{2}$.

In the observer's rest frame, in this case:

$$\sin \theta = \frac{1}{\gamma} \rightarrow \theta = \pm \arcsin(1/\gamma) \quad (2.44)$$

Therefore, observers see synchrotron radiation from the electron in a narrow beam angle $\left(\frac{2}{\gamma}\right)$ and this effect is called "Beaming effect" (Figure 2.7)



Figure 2.7: This figure shows the beaming effect which is a narrow angle for the radiation towards the observer. The dotted curve shows the original dipole power pattern of Larmor radiation and the solid line shows the case of $\gamma = 5$

The beaming effect allows observers to see a short pulse of the radiation. Note that the duration Δt_p for observing the pulse is shorter than the time Δt , which the electron passes the narrow region $\left(\frac{2}{\gamma}\right)$ because the electron moves toward the observer with the

speed $\sim c$ (Figure 2.8).

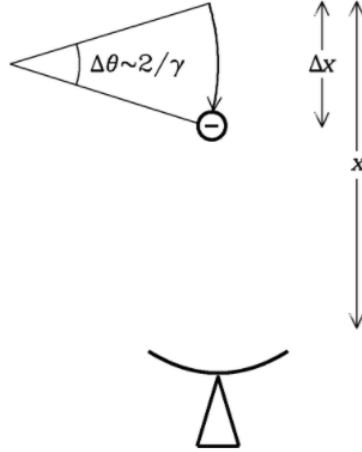


Figure 2.8: This figure shows the simple configuration of synchrotron radio source and the observer. During the time Δt the electron moves $\Delta x = v\Delta t$ toward the observer, it almost keeps up with the radiation because it is relativistic.

$$\begin{aligned}
 \Delta t_p &= t(\text{end of observed pulse}) - t(\text{start of observed pulse}) \\
 &= \frac{\Delta x}{v} + \frac{(x - \Delta x)}{c} - \frac{x}{c} \\
 &= \frac{\Delta x}{v} - \frac{\Delta x}{c} = \frac{\Delta x}{v} \left(1 - \frac{v}{c}\right) \ll \frac{\Delta x}{v} = \Delta t
 \end{aligned} \tag{2.45}$$

Replacing the total magnitude field by its perpendicular component $B_\perp = B \sin \alpha$ yields

$$\Delta t_p = \frac{1}{\gamma^2 \omega_G \sin \alpha} \tag{2.46}$$

where α is the pitch angle of the electron.

Thus the synchrotron pulse is spiky with the halfwidth $\frac{\Delta t_p}{2} < 10^{-10} s$ and the time period is $\frac{\gamma}{\gamma_G} > 10^2 s$ (Figure 2.9).

The synchrotron spectrum from a single electron is relatively flat at low frequencies and suddenly falls above

$$\nu_{\max} \sim \frac{1}{2\Delta t_p} \sim \pi \gamma^2 \nu_G \sin \alpha \propto \gamma^2 B_\perp \tag{2.47}$$

Once we know the pulse shape, we can derive the synchrotron power spectrum of a single electron by the Fourier transform as follows:

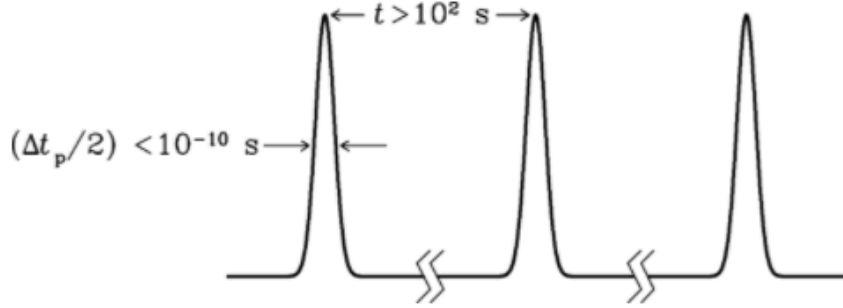


Figure 2.9: Synchrotron radiation by a single electron has a narrow pulses. Fourier transform of these pulses yields the power spectrum of synchrotron radiation (Equation 2.48).

$$P(\nu) = \frac{\sqrt{3}e^3 B \sin \alpha}{m_e c^2} \left(\frac{\nu}{\nu_c} \right) \int_{\nu/\nu_c}^{\infty} K_{5/3}(\eta) d\eta \quad (2.48)$$

where $K_{5/3}$ is a modified Bessel function and ν_c is the critical frequency:

$$\nu_c = \frac{3}{2} \gamma^2 \nu_G \sin \alpha \quad (2.49)$$

The spectrum shape of a single electron is shown in Figure 2.10.

Indeed, the property by a single electron smears out when we consider an ensemble of electrons due to a wide variety of energies and pitch angles.

2.2.1 Synchrotron Spectra of Optically Thin Radio Sources

Here I consider the situation where a synchrotron source is optically thin ($\tau \ll 1$). In this case, the spectrum of synchrotron radiation is a superposition of the spectra from individual distribution, and its flux density cannot rise faster than $\nu^{1/3}$ at any frequency ν . We usually obtain the spectral index $\alpha \sim -0.75$ (+ sign convection) from the observation for most astrophysical sources of synchrotron radiation. The energy distribution of high energy electrons is roughly a power-law from the theory of Fermi acceleration

$$n(E)dE \propto E^{-\delta}dE \quad (2.50)$$

where $m(E)dE$ is the number of electrons whose energy is between E and $E + dE$.

Here, I assume each electron emits the averaged power $\langle P \rangle$ (Equation 2.37) with any energy E

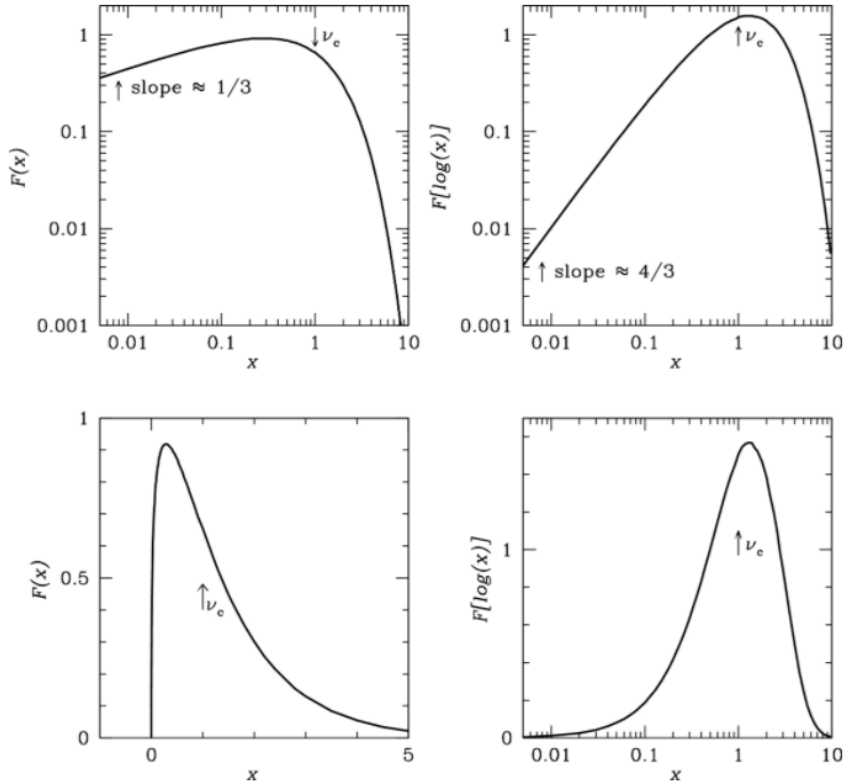


Figure 2.10: These plots show the same function $F(x) \equiv x \int_x^\infty K_{5/3}(\eta) d\eta$ where $x \equiv \nu/\nu_c$ in different ways. In the log-log plot (upper left), we can see the spectral index is $1/3$ less than $x = 1$ and it significantly falls above that.

$$P = -\frac{dE}{dt} = \frac{4}{3}\sigma_T\beta^2\gamma^2cU_B \quad (2.51)$$

at frequency $\nu \sim \gamma^2\nu_G$, which is close to the critical frequency ν_c (Equation 2.49). Then the emission coefficient of synchrotron radiation by an ensemble of electrons is

$$j_\nu d\nu = -\frac{dE}{dt}n(E)dE \quad (2.52)$$

where $E = \gamma m_e c^2 \sim \left(\frac{\nu}{\nu_G}\right)^{1/2} m_e c^2$.

Then we can write

$$dE \approx \frac{m_e c^2 \nu^{-1/2}}{2\nu_G^{1/2}} d\nu \quad (2.53)$$

so,

$$j_\nu \propto \left(\frac{4}{3}\sigma_T\beta^2\gamma^2cU_B\right) (E^{-\delta}) \left(\frac{m_e c^2 \nu^{-1/2}}{2\nu_G^{1/2}}\right) \quad (2.54)$$

To investigate the frequency dependence of the emission coefficient j_ν on the frequency ν and the magnetic field B , I eliminate E and ν_G from the equation above, then

$$\begin{aligned} j_\nu &\propto \left(\frac{\nu}{\nu_G}\right) B^2 \left(\frac{\nu}{\nu_G}\right)^{-\delta/2} (\nu\nu_G)^{-1/2} \propto \left(\frac{\nu}{B}\right) B^2 \left(\frac{\nu}{B}\right)^{-\delta/2} (\nu B)^{-1/2} \\ &\propto B^{(\delta+1)/2} \nu^{(1-\delta)/2} \end{aligned} \quad (2.55)$$

Consequently, the synchrotron radiation in the case of optically thin with the power-law distribution ($n(E) \propto E^{-\delta}$) also has a power-law distribution and its spectral index $\alpha = \frac{1-\delta}{2}$.

In our galaxy, we observe $\alpha \sim -0.75$ around 1 GHz and then $\delta \sim 2.5$.

2.2.2 Synchrotron Self-Absorption

The brightness temperature of synchrotron sources cannot exceed an absolute value at low frequencies, although most radio sources have the emission coefficient $j_\nu \propto \nu^\alpha$ (mostly in the case of optically thin: $\alpha \sim -0.75$). If electrons in LTE and they have the Maxwellian energy distribution, they are thermal sources and their brightness temperatures equal to the electron's kinetic energy.

Here, I describe in the case where electrons are optically thick ($\tau \ll 1$). In this case, synchrotron self-absorption happens and spectral index changes into $\alpha = \frac{5}{2}$.

2.2. SYNCHROTRON RADIATION

Firstly, I assume the critical frequency where most of the electrons with energy $E = \gamma m_e c^2$ emit the synchrotron radiation

$$\nu_c \sim \frac{\gamma^2 e B}{2\pi m_e c} \quad (2.56)$$

In the relativistic gas, the ratio between specific heats at constant pressure and volume is $\frac{c_p}{c_v} = \frac{4}{3}$ (nonrelativistic case: $\frac{5}{3}$). So the relation between electron energy E and electron temperature T_e is

$$E = 3kT_e \quad (2.57)$$

Thus, the effective temperature of relativistic electrons is defined below:

$$T_e \equiv \frac{E}{3k} = \frac{\gamma m_e c^2}{3k} \quad (2.58)$$

Eliminating γ from Equation 2.56 and 2.58 yields

$$T_e \approx \left(\frac{2\pi m_e c \nu}{e B} \right)^{1/2} \frac{m_e c^2}{3k} \sim 1.18 \times 10^6 \left(\frac{\nu}{\text{Hz}} \right)^{1/2} \left(\frac{B}{\text{gauss}} \right)^{-1/2} \quad (2.59)$$

At sufficiently low frequency, the brightness temperature T_b approaches the effective electron temperature T_e , and radio sources become opaque. In the Rayleigh-Jeans limit, we can write T_b as follows:

$$T_b \equiv \frac{I_\nu c^2}{2k\nu^2} \quad (2.60)$$

where I_ν is the spectral brightness.

Substituting $T_b \sim T_e$ and Equation 2.59 yields:

$$I_\nu \sim \frac{2kT_e \nu^2}{c^2} \propto \nu^{1/2} \nu^2 B^{-1/2} = \nu^{5/2} B^{-1/2} \quad (2.61)$$

Therefore, the self-absorbed synchrotron source has a spectral index $\alpha \sim \frac{5}{2}$ ($S(\nu) \sim \nu^{5/2}$), which is independent of the slope δ .

The spectrum of a homogeneous cylindrical synchrotron source is showed in Figure 2.11.

However, real radio sources have more complex shapes because they have nonuniform magnetic fields and electron energy distributions (Figure 2.12).

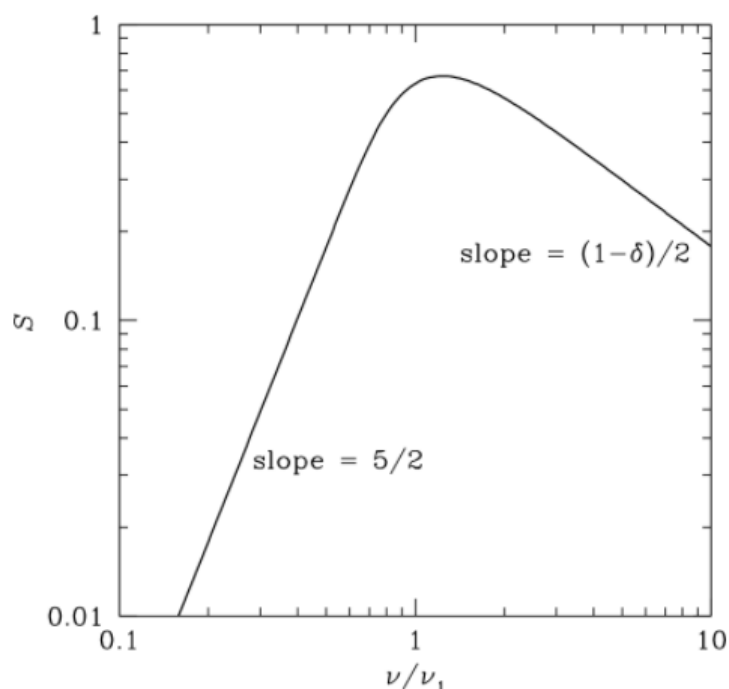


Figure 2.11: This figure shows the synchrotron spectrum. ν_1 is the frequency at which $\tau = 1$. The spectral index at the frequency ν above ν_1 is $(1 - \delta)/2$. At lower frequencies less than ν_1 , we can see the synchrotron self-absorption with the slope $5/2$.

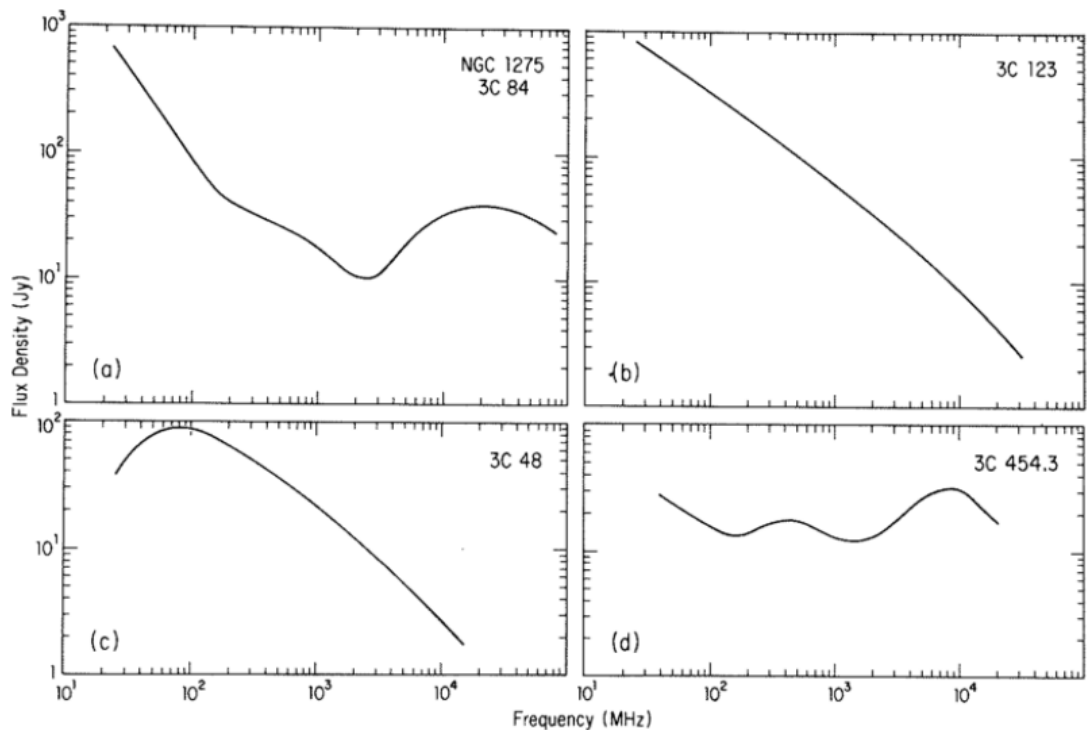


Figure 2.12: These plots show the radio spectra at low frequencies ($10 \sim 10^5$ MHz). Since real radio sources do not have uniform structures, these spectra look quite different from the uniform case (Figure 2.11)

Chapter 3

Data

In this chapter, I describe the dataset used for our study. In Section 3.1, I introduce the Herschel Reference Survey Catalog (Boselli et al. 2010). Here, I explain how they choose galaxies for the catalog and previous studies for them. In Section 3.2, I introduce the GaLactic Extragalactic All-sky MWA survey, which we obtained the radio data for galaxy samples.

3.1 Herschel Reference Survey (HRS)

In this section, I introduce the Herschel Reference Survey (HRS) catalog (Boselli et al. 2010) from which we selected galaxy samples. This survey is one of the Herschel guaranteed time key projects, and originally it was compiled for understanding dust properties and the interstellar medium in nearby galaxies. The catalog is publicly available and contains 322 galaxies selected with three criteria as follows:

1. Volume-limited:

They choose galaxies whose distance from the earth is between 15 and 25 Mpc. This limitation reduces the distance uncertainty due to the galaxy peculiar motions and the selection effect due to the high- z galaxies. The lower limit (15 Mpc) also helps us to observe sources within reasonable exposure time because very close galaxies are extended, and we need too much time for the observation.

2. K -band selection:

They choose galaxies whose 2MASS K -band total magnitudes are brighter than

CHAPTER 3. DATA

12 mag for star-forming and peculiar galaxies (Sa-Sd-Im-BCD), and 8.7 mag for quiescent galaxies (E, S0, S0a). If there are galaxies whose K -band magnitude darker than those values, their measurements are not regarded as accurate photometry because of not enough exposure time. The reason why they have selected quiescent galaxies with the more stringent K -band selection criteria is these galaxies are expected to have low dust contents, and it is difficult to detect within the reasonable exposure time.

3. High galactic latitude:

They choose galaxies whose galactic latitude is high enough to minimize the contamination from the galactic center ($b > +55^\circ$). Also, they select galaxies with the low galactic extinction ($A_B < 0.2$; Schlegel et al. 1998).

The selected galaxies locate in the sky region between $10^{\text{h}}17^{\text{m}} < \text{R.A.}(2000) < 14^{\text{h}}43^{\text{m}}$ and $-6^\circ < \text{decl.} < 60^\circ$ (Figure 3.1). HRS galaxies span a wide range of the galaxy density environment from the center of the Virgo cluster to the isolated region. As a definition, we can regard the HRS sample as an ideal one for studying the galaxy environment.

In addition to a wide range of the environment, HRS galaxies distribute a wide range of galaxy morphology (Figure 3.2).

Since HRS galaxies are supposed to be well-represented for the whole galaxy population located in the local universe, investigating their physical properties is crucial to understand them. After Boselli et al. (2010) published the HRS catalog, many studies investigating the physical properties for HRS galaxies have been done until now. Here, I introduce some of the studies for the HRS sample. Cortese et al. (2012) investigated their UV and optical properties using the Galaxy Evolution Explorer (*GALEX*; Martin et al. 2005) and SDSS-DR7 (Abazajian et al. 2009). Boselli et al. (2014) studied their cold gas properties with ^{12}CO (1 – 0) observed by the Kitt Peak 12m radio telescope and obtained from the literature data. They also investigate the HI gas obtained from The Arecibo Legacy Fast ALFA (ALFALFA; Giovanelli et al. 2005; Haynes et al. 2011) survey. Ciesla et al. (2014) executed the SED fitting for HRS galaxies with Code Investigating GALaxy Emission (CIGALE; Noll et al. 2009).

Thanks to all of the previous research about the HRS sample, they are well-studied from the X-ray to the radio emission at 1.5 GHz. However, the low-frequency around 100 MHz is not examined so far. Since we extend the wavelength range of the HRS sample to around 100 MHz, in this study, we focus on a subsample of HRS galaxies whose counterpart is detected by the latest low-frequency survey (Section 3.2).

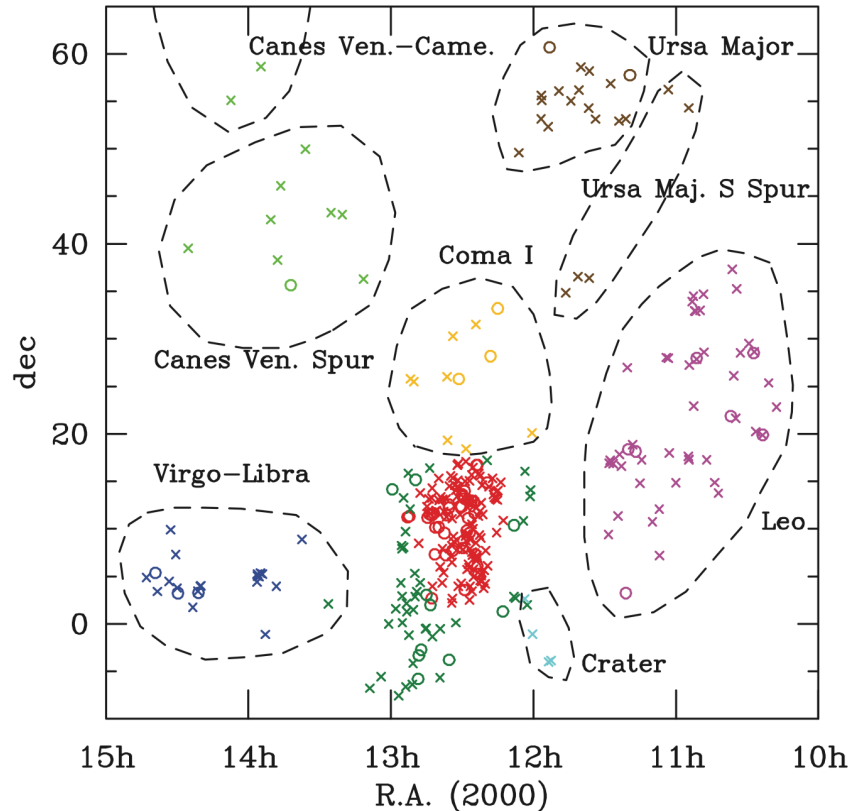


Figure 3.1: (Reprint from Boselli et al. 2010, Figure 1)

This figure shows the sky distribution of HRS galaxy samples. They show the early-type galaxies (E, S0, S0a) and late-type galaxies with circles and crosses, respectively. Dashed circles represent the different cloud regions. Each name of the cloud is shown close to each region. The red and dark green markers are Virgo galaxies (red: Virgo center, dark green: its outskirts).

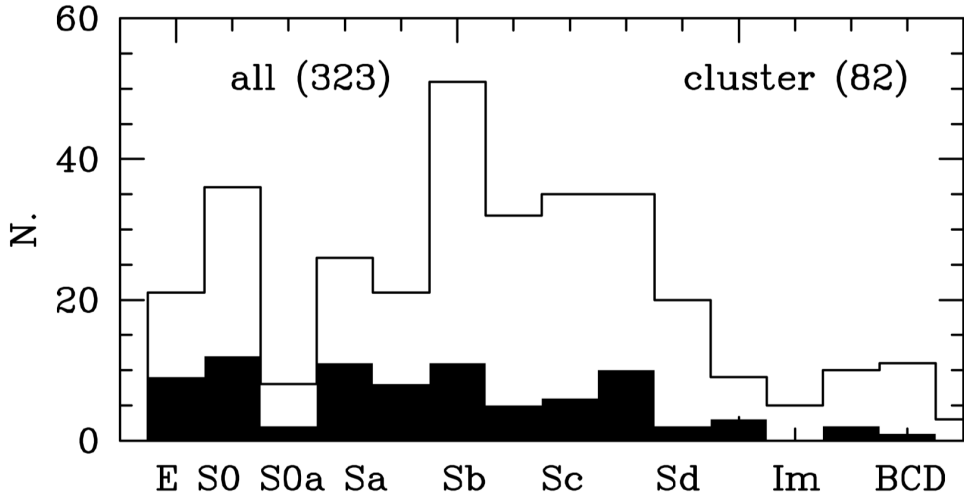


Figure 3.2: (Reprint from Boselli et al. 2010, Figure 2)

This figure shows the distribution in the morphology-type of HRS galaxies. The shaded histogram represents the distribution in it of only the cluster sample. Here, the cluster sample composed of HRS galaxies located in the Virgo A and B clouds.

3.2 GLEAM survey

In this section, I introduce the GaLactic Extragalactic All-sky MWA (GLEAM) survey (Hurley-Walker et al. 2017) which we obtained the radio continuum data from. This survey was operated by the Murchison Widefield Array (MWA) telescope in Western Australia (Tingay et al. 2013). It observed a whole southern sky and a northern sky up to $+30^\circ$ ($\sim 25,000 \text{ deg}^2$; Figure 3.3). The catalog from this survey is a publicly-available and contains 307,455 detected radio sources with fluxes at 20 narrow bands between 72 and 231 MHz (each band has 7.68 MHz band width). The sensitivity and angular resolution at 200 MHz are $\sim 7 \text{ mJy}$ and $\sim 2 \text{ arcmin}$ respectively. The completeness of this survey at 200 MHz is 90% at $\sim 170 \text{ mJy}$. Since this survey allows us to examine the low-frequency spectral energy distribution accurately with its 20 narrow bands, we adopt the radio source catalog for our study.

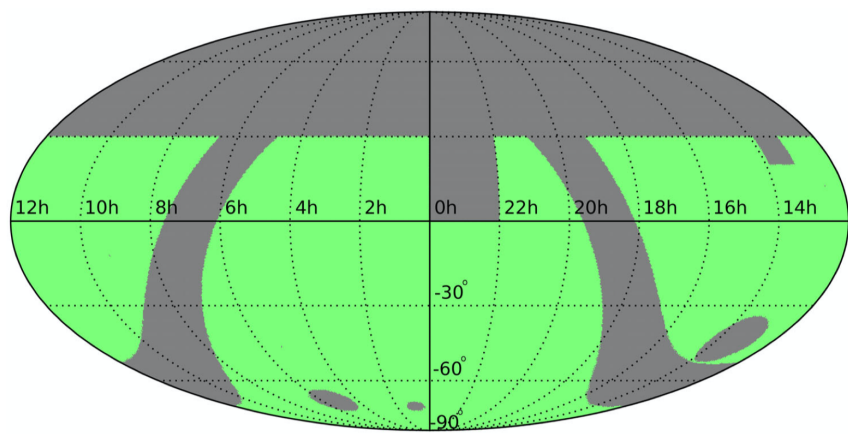


Figure 3.3: (Reprint from Hurley-Walker et al. 2017, Figure 11)

This figure shows the observed area by the GLEAM survey (green shaded region). Hurley-Walker et al. (2017) exclude several regions intentionally to minimize the contamination: Galactic plane (Absolute Galactic latitude $< 10^\circ$), Ionospherically distorted ($0^\circ < \text{Dec} < +30^\circ$ and $22^\text{h} < \text{R.A.} < 0^\text{h}$), Centaurus A ($13^\text{h}25^\text{m}28^\text{s} - 43^\circ01'09''$, $r = 9^\circ$), Sidelobe reflection of Cen A ($20^\circ < \text{Dec} < +30^\circ$ and $13^\text{h}07^\text{m} < \text{R.A.} < 13^\text{h}53^\text{m}$), Large Magellanic Cloud ($05^\text{h}23^\text{m}35^\text{s} - 69^\circ45'22''$, $r = 5.5^\circ$) and Small Magellanic Cloud ($00^\text{h}52^\text{m}38^\text{s} - 72^\circ48'01''$, $r = 2.5^\circ$).

Chapter 4

Methods

In this chapter, I describe procedures of our study from making a subsample of HRS galaxies to calculating the radio SFR. Section 4.1 and 4.2 show how to select samples from two catalogs introduced in the previous section for q_ν analysis henceforth. Section 4.3 gives the definition of q_ν and the way to apply it for our samples. Section 4.4 describes the method to estimate total IR luminosity from several IR bands' observations. Section 4.5 shows how to find the frequency dependence of q_ν by the fitting. Section 4.6 describes the process of calculating SFR from the low-frequency radio emission.

4.1 Cross Matching

Although HRS galaxies have been studied in multi-wavelength observations, their spectral energy distribution around 100 MHz is not well-understood (Ciesla et al. 2014), where the contribution from synchrotron radiation is much more significant than from free-free emission (Condon 1992). Here, I provide a procedure to cross-matching with two different catalogs I have mentioned in the previous chapter. Cross-matching is the method widely used in astronomy to obtain additional information from other surveys or catalogs by matching coordinates of each galaxy or blob source within a specific error (e.g., $\sim 1.0 \text{ arcsec}$). For executing this method for the HRS and the GLEAM survey catalog, we use Tool for OPerations on Catalogues And Tables (TOPCAT; Taylor et al. 2009). TOPCAT is a popular and useful tool for dealing with catalogs and tables, and it allows us to do the cross-matching easily, even more than two catalogs.

Initially, we assume a 10 arcsec error radius for the cross-matching since it is equivalent

CHAPTER 4. METHODS

to the value of 95% error for the astrometry in the GLEAM survey (Section 4.5.5 in Hurley-Walker et al. 2017). This matching results in a total of 18 galaxies, which are identified to have a radio counterpart. To assess the matching, we compare a separation of counterparts from the center of galaxies with coordinate uncertainties in the GLEAM catalog. For these galaxies, we find 15 of them have a separation within a 95% error radius, and others do not. Although three of them have a more significant separation compared to the error radius, we conclude that the matching for all 18 galaxies is correct by the checking of galaxy images (Appendix A). In this paper, we regard a radio blob as a counterpart if the brightest part of each blob where the inside of the contour nearest to the center, is surrounded by the D25 radius (the isophotal optical size at 25 mag arcsec⁻²; Boselli et al. 2010).

Next, we extend the error radius up to 120 arcsec, which is corresponding to the angular resolution of the GLEAM survey at 200 MHz. This operation is because the radio sources are blurred due to the angular resolution of the GLEAM survey, and the location of them might be shifted. We know 120 arcsec error radius is quite big for the matching, but this trial gives us the inspiration for the cross-matching with blurred radio sources in the future study. The cross-matching with the error of 120 arcsec suggests that there are 25 new galaxies have a potential counterpart. To assess these matching, we look at galaxy images one by one (All galaxy images are in Appendix A). With the same condition mentioned above, we identify 21 matches for these galaxies.

Although we have identified a total of 39 matches in the same way, there are six suspicious matches because of interacting counterparts (HRS4, 216, 244, 284) and quite large separations (HRS200, 295) (Figure A.5). For these galaxies, we flag them as suspicious matches, and we do not use them for further analysis. The distribution of separations for galaxies showed in Figure 4.1.

We put all galaxy images cross-matched within 120 arcsec in Appendix A.

4.2 Reduce galaxy samples for the reliable analysis

In this section, we show some steps for selecting galaxies to do a secure analysis. Since we focus on the relation of galaxy radio emission with star formation activities, we should clarify the radio source and be sure that they are not originally from other sources rather than the star formation. The radio emission arisen from the star formation activities should be proportional to the SFR in a galaxy (Condon 1992; Murphy et al. 2011). However, elliptical galaxies have a stronger radio emission against their star formation.

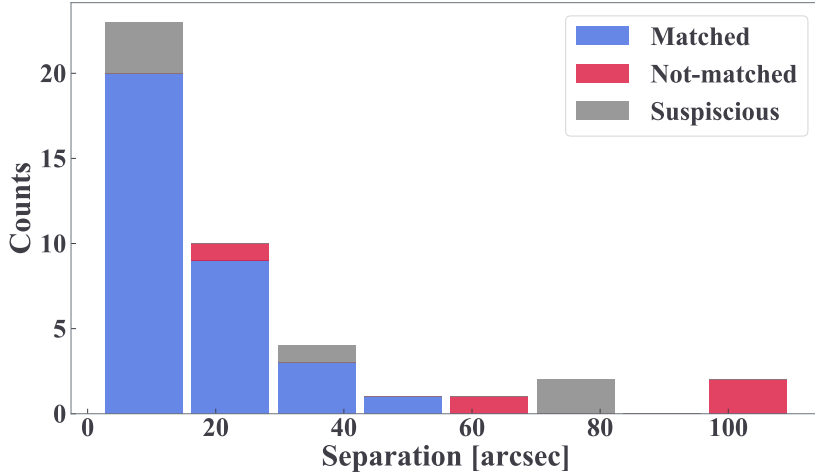


Figure 4.1: This figure shows the distribution of separations. Here we put 43 galaxies and color sorted based on the result. The blue bar shows galaxies identified to have a radio counterpart, red one does galaxies determined not to have a counterpart, and gray for the suspicious galaxies. Most of the matched samples are distributed within a 40 arcsec error radius.

In this case their radio emission would be emitted by not star-forming sources. These radio sources are considered as Active Galactic Nuclei (AGN), which emits strong radio emission due to the baryon accretion into the supermassive black hole at the center of galaxies irrelevant to the star formation (e.g., Padovani et al. 2017; Urry & Padovani 1995). According to the morphology of galaxies (Cortese et al. 2012), we identify four elliptical galaxies (HRS49, 138, 178, 241) and not use for further calculation and discussion.

After this galaxy selection, we obtain 29 galaxies with a reliable radio counterpart arisen from the star formation activity.

As a next step, we evaluate the signal to noise ratio (SNR) of radio emission at each MWA band. For reducing the uncertainty caused by observational errors, we assess the peak flux at each narrow band by comparing it to the local noise level and adopt flux values whose SNR is higher than five. This analysis results in a total of 11 galaxies have no radio fluxes whose SNR is higher than the criterion. The reason why these radio sources are detected, although they do not have any fluxes with higher SNR, is Hurley-Walker et al. (2017) determine the detection based on the SNR in the stacking images (170 – 231 MHz).

Finally, after the cross-matching and these procedures, we confirm 18 HRS galaxies are the samples available for further analysis. The overview of 18 samples is tabled in Appendix B.

4.3 Calculating the q_ν parameter

In this section, I introduce the method to calculate the q_ν parameter, which shows the ratio between integrated IR and radio luminosities in a galaxy. The definition of this parameter here is given on the following equation (e.g., Bell 2003; Calistro Rivera et al. 2017; Helou et al. 1985):

$$q_\nu \equiv \log \left(\frac{L_{8-1000\mu\text{m}} / 3.75 \times 10^{12}}{\text{erg s}^{-1} \text{Hz}^{-1}} \right) - \log \left(\frac{L_{\text{Radio},\nu}}{\text{erg s}^{-1} \text{Hz}^{-1}} \right) \quad (4.1)$$

where $L_{8-1000\mu\text{m}}$ is the total rest-frame infrared luminosity among $8 - 1000\mu\text{m}$ and $3.75 \times 10^{12}\text{Hz}$ is equivalent to the frequency of $80\mu\text{m}$ for correcting the dimension.

Although Ciesla et al. (2014) have already derived the total IR luminosity for most HRS galaxies using the SED fitting, one of our galaxy samples (HRS163) does not have the value because of the lack of the reliable mid-IR flux from *Spitzer* telescope. For consistency, we adopt the total IR luminosity calculated from the same method for all galaxy samples. To calculate the total IR luminosity, we refer to Galametz et al. (2013), which derives the calibration relation of the total IR luminosity with monochromatic IR luminosities. We show the procedure to calculate total IR luminosity in the next section.

4.4 Total IR luminosity

In this section, I present how to calculate the total IR luminosity. For the method of calculating total IR luminosity, we refer to Galametz et al. (2013), which shows the empirical relations to estimate total IR from *Spitzer* ($24, 70\mu\text{m}$) and *Herschel* bands ($100, 160, 250\mu\text{m}$). HRS galaxies have flux data from the Multiband Imaging Photometry for *Spitzer* (MIPS; Bendo et al. 2012; Rieke et al. 2004), the *Herschel*/PACS ($100, 160\mu\text{m}$; Cortese et al. 2014) and the *Herschel*/SPIRE ($250\mu\text{m}$; Ciesla et al. 2012).

Galametz et al. (2013) derived the calibration equation below:

$$L_{3-1100\mu\text{m}} = \sum c_i \nu L_\nu(i) \quad (4.2)$$

where $L_{3-1100\mu\text{m}}$ is the total IR luminosity in the frequency range from 3 to $1100\mu\text{m}$, c_i is the coefficients at $i = 24, 70, 100, 160, 250\mu\text{m}$, and L_ν is the luminosity at the frequency ν corresponds to a specific wavelength i . For deriving L_ν , we calculate it from fluxes and the distance to each galaxy. We refer to Cortese et al. (2012) for obtaining galaxy distances.

Galametz et al. (2013) derived the conversion equation with at least two bands. Therefore, we can estimate total IR luminosities even if galaxies are lack of a few fluxes. Since several calculations in the following sections require the total IR luminosity among $8 - 1000 \mu\text{m}$ ($L_{8-1000\mu\text{m}}$), we recalibrate this luminosity by multiplying the constant value (0.88) in Takeuchi et al. (2005).

The total IR luminosity calculated here is consistent with that of Ciesla et al. (2014) within factor 2 (Figure 4.2).

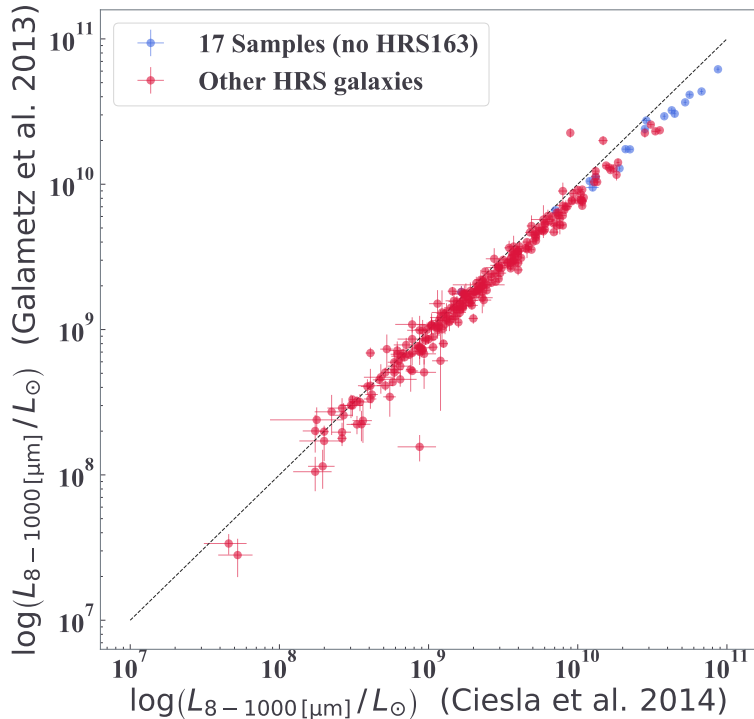


Figure 4.2: This figure shows the comparison of total IR luminosity at $8 - 1000 \mu\text{m}$ from different methods. Here, we show all HRS galaxies which have both luminosities. Blue plots show galaxy samples selected in Section 4.1 and 4.2, and red ones show other HRS galaxies. The difference of both luminosities is less than factor 2.

Hereafter, we use $L_{8-1000\mu\text{m}}$ obtained here to calculate the q parameter and SFR.

4.5 Fitting to q_ν parameters

Here, we show how to do the fitting to q_ν . At low frequencies around 100 MHz, the synchrotron emission can be dominant, which emitted from high energy electrons accelerated

CHAPTER 4. METHODS

by the supernova remnant. In this paper, we assume radio emission has a single power-law on the frequency and adopt the following equation:

$$q_\nu = -\gamma \log \nu + \beta \quad (4.3)$$

where q_ν is defined by Equation 4.1 at ν MHz, γ is the power-law index showing the frequency dependence of q_ν , and β is the second fitting parameter.

In this study, we execute two types of fitting:

1. Fitting to only MWA frequencies (72 – 231 MHz)
2. Fitting to 1500 MHz besides MWA frequencies

The flux data at 1500 MHz is obtained from Boselli et al. (2015), and here we use only high-quality flux data (flag = 1). These two types of fitting might allow us to judge the correctness of a single power-law assumption. These fitting results are summarized in Section 5.1.

4.6 Calculating the SFR

In this section, I describe how to derive SFR from low-frequency radio emissions. Here, we estimate the radio SFR, combining Equation 4.1 with the following equations:

$$\text{SFR}_{\text{IR}} = 3.88 \times 10^{-44} \left(\frac{L_{8-1000\mu\text{m}}}{\text{erg s}^{-1}} \right) \quad (4.4)$$

$$q_{\nu \text{ MHz}} = q_{1500 \text{ MHz}} + \log \left(\frac{\nu \text{ MHz}}{1500 \text{ MHz}} \right)^\gamma \quad (4.5)$$

Equation 4.4 calculates SFR from the total IR emission in Murphy et al. (2011), and Equation 4.5 shows the difference of the q_ν between a certain wavelength ν and 1500 MHz.

Substituting equation 4.1 and 4.5 into equation 4.4 yields the following equation to estimate SFR from radio emission at ν MHz:

$$\text{SFR}_{\text{Radio}, \nu} = 1.46 \times 10^{-31} \times 10^{q_{1500 \text{ MHz}}} \left(\frac{\nu \text{ MHz}}{1500 \text{ MHz}} \right)^{-\gamma} \times L_{\text{Radio}, \nu} \quad (4.6)$$

In Section 5.2, I show the results of calculating SFR from the low-frequency radio using this equation and comparing it with the SFR from other indicators.

Chapter 5

Results

In this chapter, I present our results with figures. Firstly, in Section 5.1, I show the q_ν frequency dependence for each galaxy with the distribution of γ . Secondly, in Section 5.2, I show the result of the comparison between the SFR from a radio emission and other indicators.

5.1 Distributions of γ

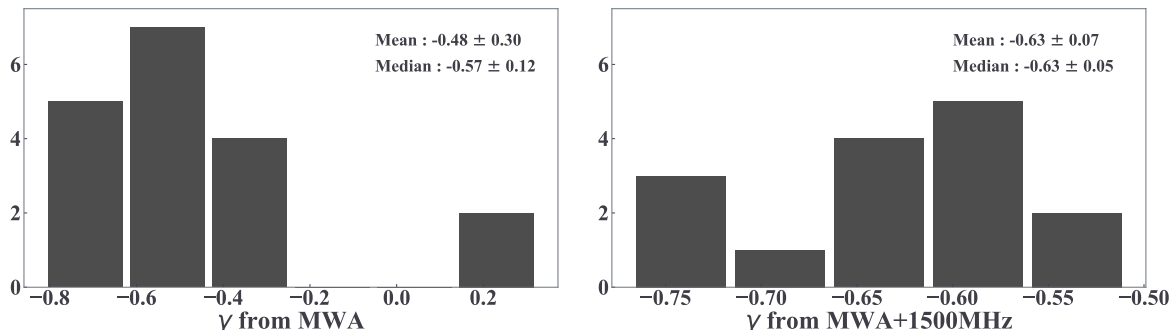


Figure 5.1: This figure shows distributions of γ for each fitting. The left figure indicates the fitting result with only MWA frequencies, and the right one does with 1500 [MHz] besides MWA frequencies.

Here, we show two kinds of fitting results. The left plot in Figure 5.1 is the γ distribution from the fitting only to MWA frequencies, and the right one is to 1500 MHz besides

CHAPTER 5. RESULTS

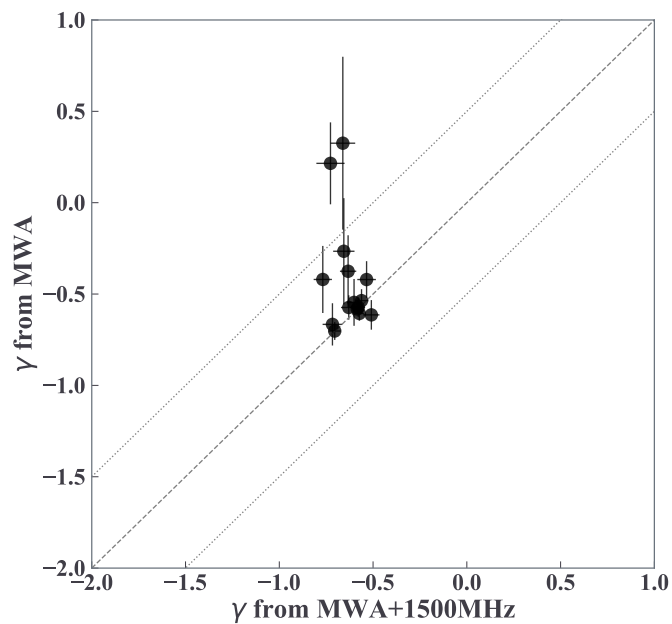


Figure 5.2: This figure is for comparing the difference of γ for each fitting method. The solid line shows the one to one correlation, and dotted lines show 0.5 dex away from the solid line. Each plot shows each galaxy. In this figure, we can see γ fitted to only MWA frequencies are relatively flatter.

5.2. COMPARING SFR INDICATORS

MWA frequencies. We show the mean and median with the standard and quantile deviation in both plots. Since we adopt high-quality flux data at 1500 MHz (Boselli et al. 2015), three samples (HRS 122, 163 and 204) are fitted only in the case with MWA fluxes. Figure 5.2 compares γ from different fitting fluxes for each galaxy.

In these figures, we can find that there are two galaxies (HRS 25 and 144) with a relatively flatter γ fitted only to MWA frequencies. This result suggests that there is a critical frequency where the turnover arises between MWA frequencies and 1500 MHz. At low frequencies, the spectral is prone to be flatter due to the free-free absorption (e.g., Calistro Rivera et al. 2017; Chyžý et al. 2018; Schober et al. 2017). In addition to this, Schober et al. (2017) show that a Milky Way like galaxy (similar SFR) has the critical frequency order of magnitude lower than the MWA frequency. However, HRS 25 and 144 have a Milky Way like SFR (Boselli et al. 2015) and a critical frequency between MWA frequencies and 1500 MHz. This result cannot be explained by Schober et al. (2017). One possible explanation is that fewer number of fluxes yields less constraint of the fitting and the flatter γ for HRS 25 and the galactic nuclei affects the spectral for HRS 144 identified as a Seyfert galaxy from the BPT diagram (e.g., Baldwin et al. 1981; Kauffmann et al. 2003; Kewley et al. 2001; Schawinski et al. 2007). The BPT diagram demonstrates to identify LINER, Seyfert galaxies from the normal star-forming one using optical line emissions. For understanding these galaxies, we would need the case study with more data in a wide frequency range.

If we neglect these galaxies, the mean γ changes from -0.48 ± 0.30 to -0.57 ± 0.14 for the fitting without 1500 MHz and from -0.63 ± 0.08 to -0.62 ± 0.08 with 1500 MHz. The mean γ does not vary in any case with 1500 MHz. This result means that HRS 25 and 144 do not affect the fitting result among MWA frequencies and 1500 MHz, although they do the mean γ from the fitting only to MWA frequencies. Therefore, in this paper, we adopt the averaged γ obtained from the fitting across the MWA frequency to 1500 MHz for calculating SFR (Section 5.2).

The fitting results are shown in Appendix C.

5.2 Comparing SFR indicators

Here, we show the result from comparing $SFR_{\text{Radio}, \nu}$ defined by Equation 4.6 with SFR_{IR} (Equation 4.4) and $SFR_{\text{FUV}+24\text{mic}}$ (Boselli et al. 2015).

Figure 5.3 shows the SFR ratio between $SFR_{\text{Radio}, \nu}$ and SFR_{IR} . For drawing the upper figure, we substitute the individual $q_{1500\text{MHz}}$ and γ into Equation 4.6. We calculate

CHAPTER 5. RESULTS

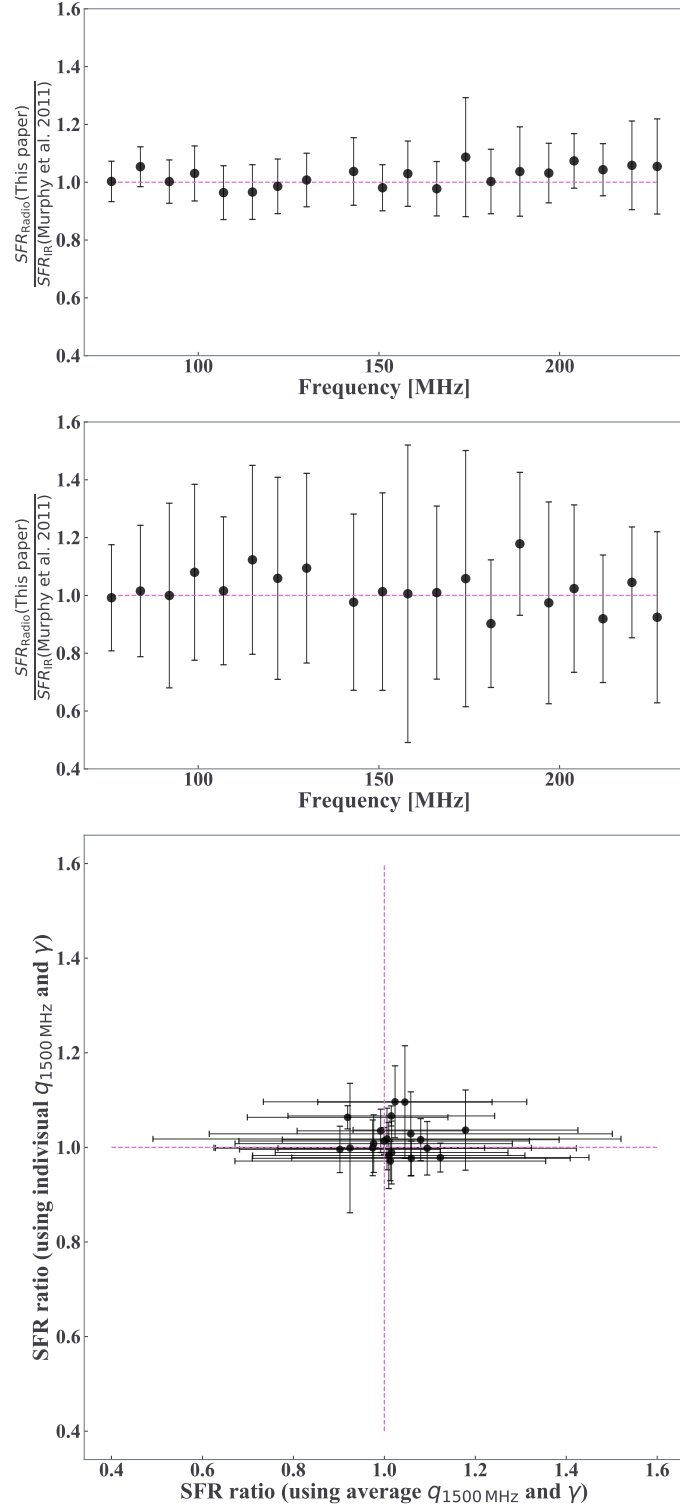


Figure 5.3: This figure shows the SFR ratio between $SFR_{\text{Radio},\nu}$ and SFR_{IR} at each MWA frequency. The difference between the upper and middle plots is the calibration parameters to calculate $SFR_{\text{Radio},\nu}$. Individual or averaged γ and $q_{1500 \text{ MHz}}$ are used for the upper or middle plots, respectively. The bottom plot compares SFR ratios calculated with different calibrations.

5.2. COMPARING SFR INDICATORS

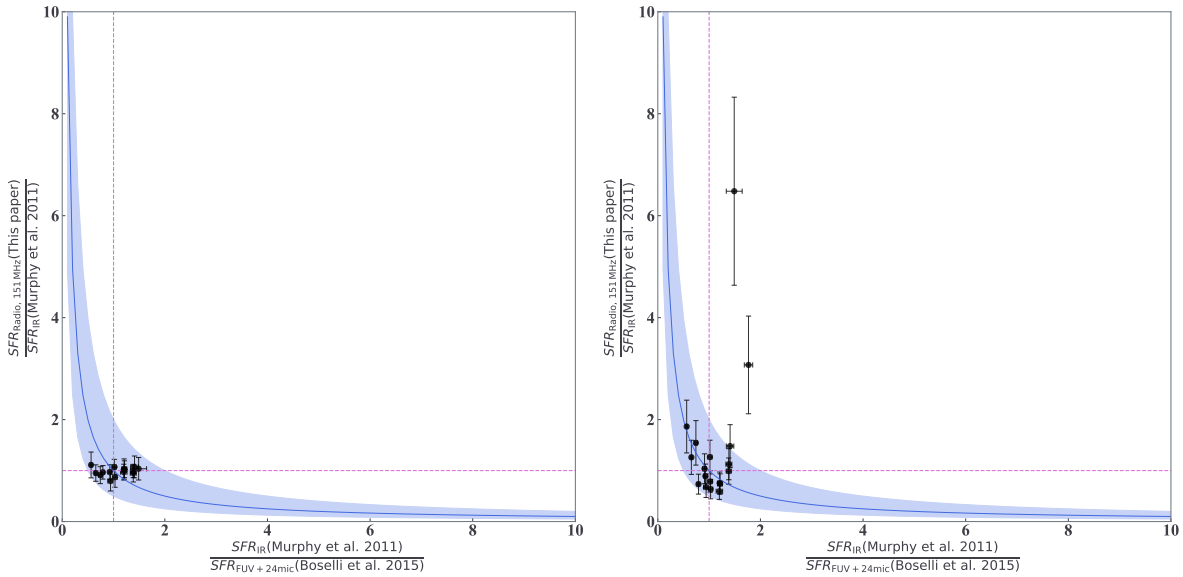


Figure 5.4: This figure shows SFR ratios from different indicators. The vertical and horizontal axes are $SFR_{\text{Radio}, 151 \text{ MHz}} / SFR_{\text{IR}}$ and $SFR_{\text{IR}} / SFR_{\text{FUV} + 24\text{mic}}$ in both plots. Magenta dashed lines indicate the unity for each SFR ratio, and the solid blue lines do for the SFR ratio between $SFR_{\text{Radio}, 151 \text{ MHz}} / SFR_{\text{FUV} + 24\text{mic}}$. The blue shaded region shows the ratio between $SFR_{\text{Radio}, 151 \text{ MHz}}$ and $SFR_{\text{FUV} + 24\text{mic}}$ within factor two ($0.5 \leq SFR_{\text{Radio}, 151 \text{ MHz}} / SFR_{\text{FUV} + 24\text{mic}} \leq 2$). The difference between the upper and middle plots is the calibration parameters to calculate $SFR_{\text{Radio}, 151 \text{ MHz}}$.

CHAPTER 5. RESULTS

$\text{SFR}_{\text{Radio}, \nu}$ at each MWA frequency, and plot the mean value. Note that the number of galaxies taken for the mean at each frequency is different because we use only high-quality fluxes. In this case, we can see it is consistent with SFR_{IR} within a 10% error. For the middle figure, we substitute the averaged $q_{1500 \text{ MHz}}$ and γ instead of individual values. This calibration method yields larger scatters compared to the previous one. However, $\text{SFR}_{\text{Radio}, \nu}$ is still consistent with SFR_{IR} . The bottom figure shows the SFR ratio comparison from different calibrations. In this figure, it is clear that SFR calculated from the averaged value has more extensive scatters than from the individual values.

These figures give us the idea that calculating radio SFR needs the spectral energy distribution for less uncertainty. For the spectral, we find that the single power-law assumption yields the radio SFR with the consistency within 10%, even including galaxies that might have a flatter spectral at low frequencies.

Figure 5.4 shows the comparison of SFR ratios. For both plots in the figure, vertical and horizontal axes show the ratio between $\text{SFR}_{\text{Radio}, 151 \text{ MHz}}$ and SFR_{IR} , between SFR_{IR} and $\text{SFR}_{\text{FUV}+24\text{mic}}$, respectively. We use radio emission at 151 MHz because this is the only flux band that all our samples have high-quality data. Here, we check the consistency of the radio SFR with other SFR indicators. While SFR_{IR} traces the only dust emission, $\text{SFR}_{\text{FUV}+24\text{mic}}$ does the direct young massive stellar emission dust-corrected with the radiation at 24 μm (Kennicutt & Evans 2012; Murphy et al. 2011). This figure shows how consistent the radio SFR is with this direct emission tracer. The difference between these plots is the calibration parameter for calculating $\text{SFR}_{\text{Radio}, 151 \text{ MHz}}$. The individual $q_{1500 \text{ MHz}}$ and γ are used for the left plot and the averaged ones for the right plot. The blue shaded region shows the ratio between $\text{SFR}_{\text{Radio}, 151 \text{ MHz}}$ and $\text{SFR}_{\text{FUV}+24\text{mic}}$ within factor two ($0.5 \leq \text{SFR}_{\text{Radio}, 151 \text{ MHz}} / \text{SFR}_{\text{FUV}+24\text{mic}} \leq 2$). In the figure, we can see that the radio SFR using individual parameters is also consistent with $\text{SFR}_{\text{FUV}+24\text{mic}}$. However, in the other case, there are two galaxies (HRS 306 and 144) whose radio SFR overestimates. This is because these galaxies have stronger radio emission (lower q_ν) than the extrapolated average value at 151 MHz.

Chapter 6

Discussions

In this chapter, we show further discussion on our results in Chapter 5. Section 6.1 compares our fitting results, mainly the frequency dependence of q_ν with previous studies. Section 6.2 shows the comparison of the radio SFR calibration with Calistro Rivera et al. (2017). Section 6.3 describes how galaxy properties affect the SFR estimation. Here, we focus on the HI deficient and the active galactic nuclei in a galaxy. Section 6.4 describes HRS galaxies whose radio counterparts are not detected by the GLEAM survey. In this section, I also mention the possibility of their radio source detection by the updated GLEAM survey.

6.1 Comparing the calibration with previous results

Here, we compare our results in Section 5.1 with previous research. From our samples, we obtain the mean $\gamma = -0.63 \pm 0.07$ with MWA frequencies and 1500 MHz. Calistro Rivera et al. (2017) and Chyzy et al. (2018) obtained -0.78 ± 0.24 and -0.56 ± 0.11 , respectively.

The difference of these might result from the selection of galaxy samples. While we use nearby galaxies within 25 Mpc, Calistro Rivera et al. (2017) do 758 galaxies up to $z \sim 2$, and Chyzy et al. (2018) do 118 galaxies up to $z = 0.04$.

Chyzy et al. (2018) indicate that the slope is steeper at higher frequencies ($1.3 \sim 5$ GHz), and this might steepen the slope of galaxy samples in Calistro Rivera et al. (2017) which adopt galaxies up to $z \sim 2$. Considering the value and scatter, our result using the Herschel reference sample would be consistent with previous findings. Indeed, the frequency dependence of the low-frequency emission and its relation with IR emission

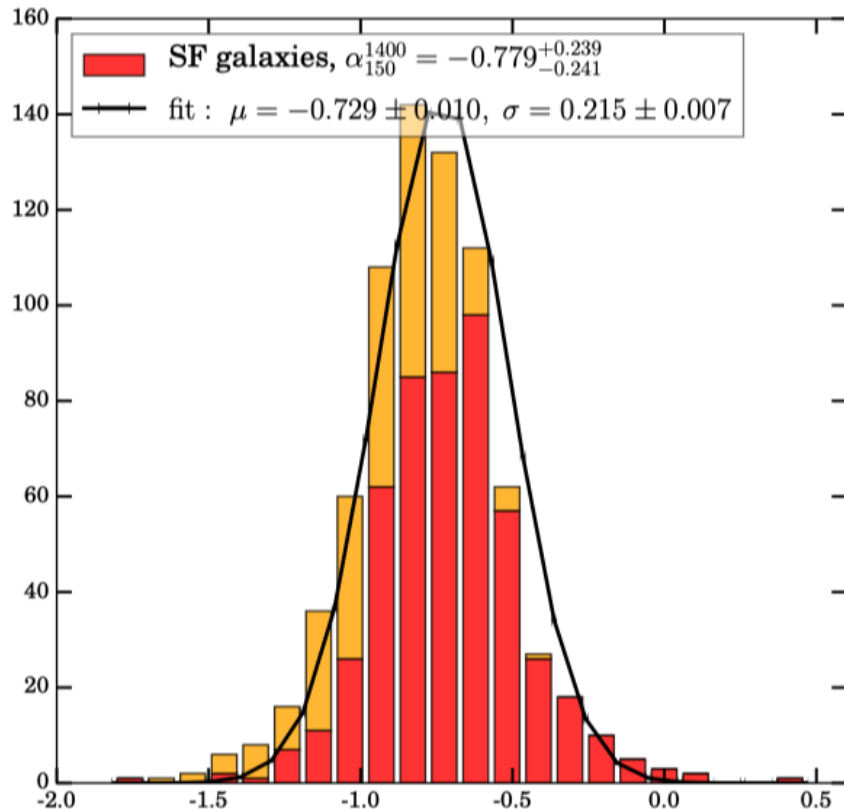


Figure 6.1: This figure shows the spectral index corresponding to γ in this paper. They calculate it between 150 MHz (LOFAR; Williams et al. 2016) and 1.4 GHz (Westerbork Synthesis Radio Telescope, WSRT; de Vries et al. 2002). Red and orange histograms show the samples detected and non-detected by WSRT. To estimate the flux of non-detected samples, they extract aperture fluxes from the source location known by LOFAR on the radio map (forced photometry technique). The black solid line displays the Gaussian fitting function. They put the average μ and standard deviation σ from the fitting on the upper right in the figure.

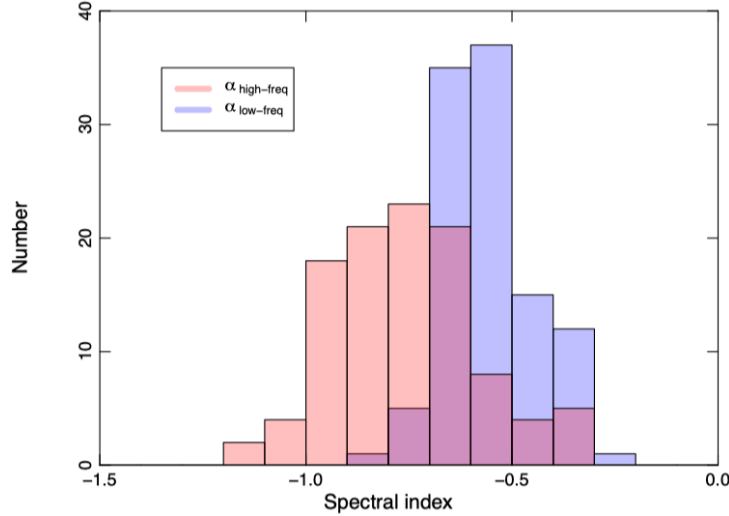


Figure 6.2: This figure shows the spectral index corresponding to γ in this paper. Red and blue histograms show the spectral index corresponding to γ in this paper calculated fluxes from 1.3 GHz to 5 GHz and 150 MHz to 1.4 GHz, respectively. They show histogram in violet where they are overlapping. From the definition, we should compare our result with the blue one. They calculate it between 150 MHz (The Multifrequency Snapshot Sky Survey, MSSS; Heald et al. 2015) and 1.4 GHz (the NRAO VLA Sky Survey, NVSS; Condon et al. 1998).

is still uncertain.

6.2 Radio SFR uncertainty

In Section 5.2, we show the consistency of our SFR calibrations using the low-frequency emission. For calculating the more accurate radio SFR, we need its spectral energy distribution for each galaxy, as we have already shown in Section 5.2. Since star-forming galaxies have a wide variety of q_ν at low frequencies (~ 0.53 dex in Figure 14, 15; Calistro Rivera et al. 2017), and still we do not know the physical details, the radio SFR calibration has considerable uncertainty. Substituting averaged γ and $q_{1500 \text{ MHz}}$ obtained from our sample galaxies into Equation 4.6 yields the following equation:

$$\text{SFR}_{\text{Radio}, 150 \text{ MHz}} = (1.03 \pm 0.27) \times 10^{-29} \times \left(\frac{L_{\text{Radio}, 150 \text{ MHz}}}{\text{erg s}^{-1}} \right) \quad (6.1)$$

where we substitute the median values of $\gamma = -0.63$, $q_{1500 \text{ MHz}} = 2.48$ and $\nu = 150 \text{ MHz}$ into Equation 4.6.

Calistro Rivera et al. (2017) have obtained the coefficient of 0.76 ± 0.08 at $z = 0$ (Equation 11) from their calibration.

We should keep our mind that the SFR calibration has non-negligible uncertainty, possibly caused by the galaxy selection and the variety of q_ν at low frequencies. We need the radio spectral with multi-band observation for estimating SFR accurately.

6.3 Galaxy properties for the radio SFR

In this section, I discuss how the galaxy property affect the results mentioned in previous sections. Here, I focus on the central engine and the environment of a galaxy. The central engine of a galaxy driven by the supermassive black hole and the accretion is located at the center of a galaxy, and it is known to emit strong radio emission. Although we have eliminated galaxies which have strong radio emission without star formation activity in Section 4.2, there are still some galaxies in our sample, which might have strong radio emissions compared to the radiation arisen from the star formation. These kinds of galaxies that have a strong radio emission in spite of the star-forming are called Seyfert or LINER galaxies based on the strength of optical emission lines, and it is possible to affect our results due to their strong emissions. In this study, we investigate this property using the BPT diagram mentioned in Section 5.1 and find four galaxies (HRS 144, 163 and 220) in our sample that have sharp optical emission lines. In the BPT diagram, HRS 144 and 163 are found to be Seyfert galaxies, and HRS and 220 are LINER galaxies.

After that, we also examine the galaxy environment of each galaxy. Boselli et al. (2014) have already calculated the HI-deficiency for all HRS galaxies based on the calculation in Boselli & Gavazzi (2009). HI deficient galaxy is defined as a galaxy whose the HI mass is much smaller than the expected one based on the morphology and the size of a galaxy (Haynes & Giovanelli 1984). The definition of HI deficiency is as follows:

$$\text{HI-def} = \log(M_{\text{HI, expected}}) - \log(M_{\text{HI, observed}}) \quad (6.2)$$

where $\log(M_{\text{HI, expected}})$ is defined in Haynes & Giovanelli (1984):

$$\log(h^2 M_{\text{HI, expected}}) = c + d \log(h \times \text{diam})^2 \quad (6.3)$$

where c and d are weak functions of the galaxy morphology, diam is the linear diameter of the galaxy and $h = H_0/100$.

Here, we regard a galaxy whose HI deficiency is more than 0.4 as a HI deficient galaxy and the other case as a normal galaxy, which is the same criteria in Ciesla et al. (2016). HI deficiency is known to represent not only the amount of the HI mass but also a galaxy environment. This is because HI deficiency is caused by the tidal stripping or ram pressure,

6.3. GALAXY PROPERTIES FOR THE RADIO SFR

which happens in the dense region (e.g., the center of a cluster). Therefore, we can roughly assume that HI deficient galaxies are located in the dense areas, and normal galaxies are the field galaxies. The relation between a galaxy environment and low-frequency emissions are still not fully understood. Still, it is a possible scenario to distort the magnetic field and affect the strength of the synchrotron radiation due to the frozen-in of the magnetic field with the stripped HI gas.

Firstly, we show the result of a spectral index distribution (Figure 5.1) with the labeling.

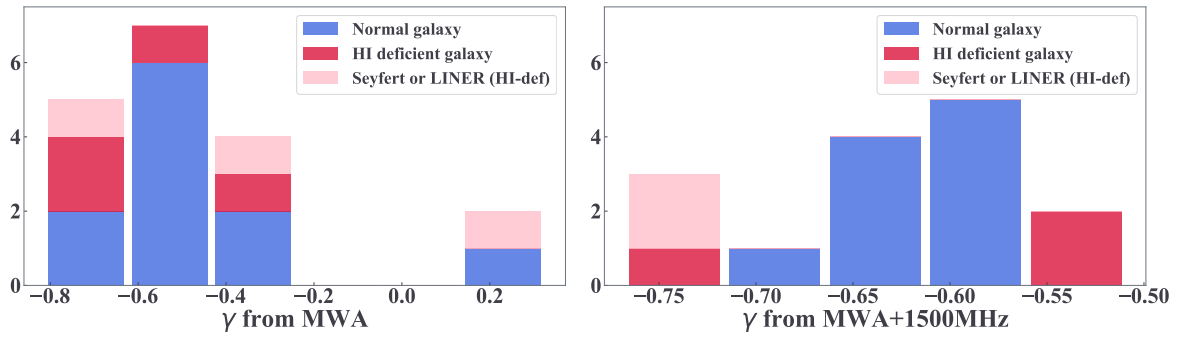


Figure 6.3: This figure shows the spectral index distribution obtained from the two kinds of fitting as same as in Figure 5.1. Here, we make a histogram with color labeling based on the galaxy properties mentioned in Section 6.3. The blue histogram shows the normal galaxies; red one shows the HI deficient galaxies ($\text{HI-def} > 0.4$), and the pink shows the Seyfert or LINER galaxies with HI-deficient. Our sample does not have the galaxy, which is Seyfert or LINER without HI deficient. Although the left figure does not show the significant difference between normal galaxies and the others, the right figure shows the HI deficient galaxies tend to have a scatter spectral index compared to the normal galaxies.

In Figure 6.3, we cannot see the significant difference between normal galaxies and the others in the left figure. But in the right one, we can see the HI deficient galaxies tend to have a scattered spectral index. This suggests that the galaxy environment might affect the energy distribution of high-energy electrons, which directly related to the spectral index. Unfortunately, in our sample, we do not find the significant difference for Seyfert or LINER galaxies, but cannot reject the possibility that these AGNs vary the spectral index.

Secondly, we show the q_ν value plots with the label. This q_ν value plot helps us to understand how the galaxy property affects the SFR ratio in Figure 5.3. As we have mentioned in Section 5.2, the q_ν value variation makes a larger scatter of SFR ratio when we estimate $\text{SFR}_{\text{Radio}, \nu}$ with averaged parameters.

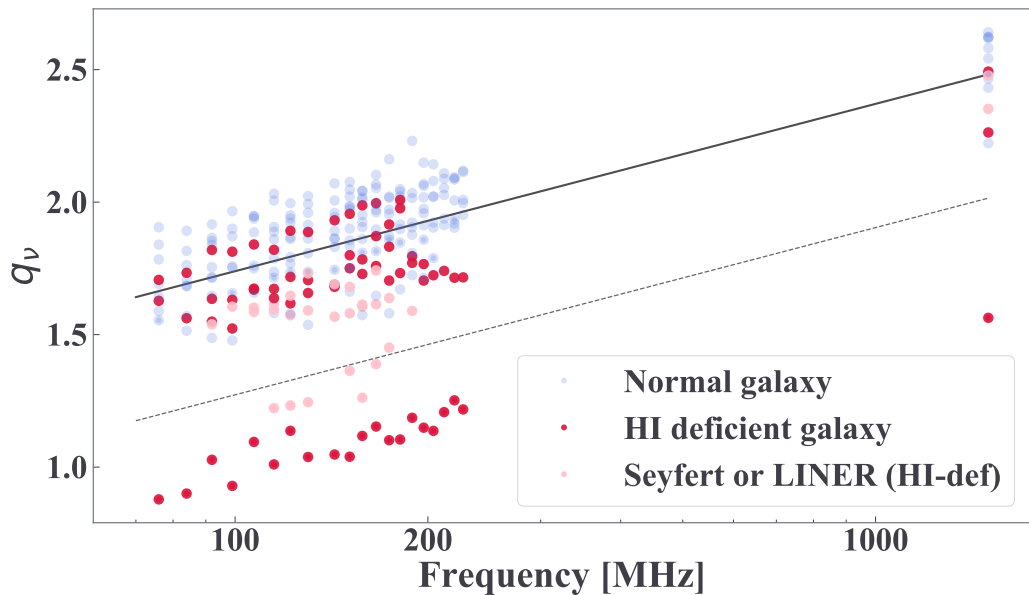


Figure 6.4: This figure shows that q_ν value distribution at MWA frequencies and 1500 MHz. The solid black line is the extrapolate line from the median value of $q_{1500 \text{ MHz}}$ to the MWA frequencies with the median spectral index γ . For calculating $\text{SFR}_{\text{Radio}, \nu}$, we have used this extrapolation. The dotted black line is the border for showing the outliers below this line. The plots below this line arise from only two galaxies, and we can say these are the outliers. In this figure, we can see the most plots distributing around the solid black line, which shows the extrapolated median value from $q_{1500 \text{ MHz}}$. But we also find there are two galaxies (HRS 163 and 306) that have lower values in a whole frequency range.

6.4. NON-DETECTED GALAXIES BY THE GLEAM SURVEY

In Figure 6.4, we can see some HI deficient galaxies and Seyfert or LINER galaxies tend to have smaller q_ν values, which means they have stronger radio emissions. We also find that there are two galaxies (HRS 163 and 306), which have significantly lower q_ν values. Since galaxies which have stronger radio emissions might possess the other radio source rather than the star formation activity, we should not estimate SFR from radio emissions for these type of galaxies. We cannot conclude how much q_ν value is safe for the SFR estimation from the low-frequency emission due to the small number of samples. In future studies, we should clarify the distribution of this plot and find the borderline for safer SFR estimation.

6.4 Non-detected galaxies by the GLEAM survey

Here, I mention galaxies that have not been observed by the GLEAM survey. In this study, we have found 39 HRS galaxies have a potential radio counterpart in the GLEAM survey in Section 4.1. Out of other 283 HRS galaxies, we confirm 44 galaxies are out of the observational region by the GLEAM survey, and HRS 183 (M87, Virgo A) is peeled because of the too strong radio emission. For other 107 galaxies that have a high-quality radio flux at 1500 MHz, we roughly compare the extrapolated flux at 200 MHz using the mean $\gamma = -0.63$ obtained in this study with the rms noise described in Hurley-Walker et al. (2017). This estimation shows that at least 34 galaxies should have been observed by the GLEAM survey.

One possible reason for the non-detection of these galaxies is a flatter radio spectral. Here, we assume $\gamma = -0.63$ for the extrapolation. However, the flux of these galaxies at 200 MHz is smaller than the expected value and the detection limit if these galaxies have a flatter spectral.

In the GLEAM-X survey, which is the follow-up observation of the GLEAM survey, more than 50 HRS galaxies will be detected even their spectral index is $\gamma = \pm 0$ because of the roughly ten times higher sensitivity of the coming up survey.

Chapter 7

Summary and Future prospects

In this study, we investigated how the relation between radio emission and star-formation activity varies across the low frequencies and the consistency of the radio SFR. For this study, we selected star-forming galaxies and their radio data from the HRS catalog (Boselli et al. 2010) and the GLEAM survey catalog (Hurley-Walker et al. 2017), respectively. We found that 18 star-forming galaxies in the HRS catalog have a radio counterpart in the GLEAM survey.

Here, I summarize our results and prospects as follows:

1. We found that a single power-law fitting was valid for modeling the relation of radio with IR luminosities from MWA frequencies ($72 \sim 231$ MHz) to 1.5 GHz. The mean of γ , which shows the frequency dependence of q_ν , is -0.63 ± 0.07 . The result is consistent with Calistro Rivera et al. (2017); Chyzy et al. (2018) within the error. The difference of the mean value among these results might be attributed to the selection of galaxy samples.
2. We checked the consistency of the SFR calculated from the low-frequency radio emission was consistent with SFRs obtained from IR luminosities. Our result also showed that the radio SFR had less scatter when we used the fitting result of each galaxy as the calibration for the indicator than the averaged quantities for calibration from all sampled galaxies. The former method had two times less scatter than the latter.
3. We also confirmed that the radio SFR was consistent with the SFR obtained from FUV dust corrected by the IR emission at $24\mu\text{m}$. Although this indicator traces the direct stellar radiation from young massive stars and possibly different from the SFR_{IR} , the radio SFR with individual parameters was consistent also with

CHAPTER 7. SUMMARY AND FUTURE PROSPECTS

$SFR_{\text{FUV+24mic}}$ within a factor of 2. We also found that calculating the radio SFR with the averaged parameters brings overestimation for some galaxies whose q_ν is significantly smaller than that of other galaxies.

4. The galaxy properties, such as the central engine and the HI deficiency, possibly affect the mean value of γ and the SFR estimation. However, it is still difficult to distinguish those galaxies from only q_ν values at present. We need to investigate the relation of galaxy properties with radio luminosities in star-forming galaxies.
5. For further understanding of the low-frequency properties in star-forming galaxies, we need more samples from multi-band observation. The updated GLEAM survey will reveal physical details with an order of magnitude better angular-resolution and sensitivity than the latest survey.

Bibliography

- Abazajian K. N., et al., 2009, *The Astrophysical Journal Supplement Series*, 182, 543
- Abolfathi B., et al., 2018, *The Astrophysical Journal Supplement Series*, 235, 42
- Baldwin A., Phillips M. M., Terlevich R., 1981, *Publications of the Astronomical Society of the Pacific*, 93, 817
- Bell E. F., 2003, *The Astrophysical Journal*, 586, 794
- Bendo G. J., Galliano F., Madden S. C., 2012, *Monthly Notices of the Royal Astronomical Society*, 423, 197
- Blumenthal G. R., Faber S. M., Primack J. R., Rees M. J., 1984, *Nature*, 311, 517
- Boselli A., Gavazzi G., 2009, *Astronomy and Astrophysics*, 508, 201
- Boselli A., et al., 2010, *Publications of the Astronomical Society of the Pacific*, 122, 261
- Boselli A., Cortese L., Boquien M., Boissier S., Catinella B., Lagos C., Saintonge A., 2014, *Astronomy and Astrophysics*, 564, 1
- Boselli A., Fossati M., Gavazzi G., Ciesla L., Buat V., Boissier S., Hughes T. M., 2015, *Astronomy & Astrophysics*, 579, A102
- Buat V., 1991, *Astrophysical Journal*, 376, 95
- Calistro Rivera G., et al., 2017, *Monthly Notices of the Royal Astronomical Society*, 469, 3468
- Carilli C. L., Holdaway M. A., Ho P. T. P., de Pree C. G., 1992, *The Astrophysical Journal*, 399, L59
- Chabrier G., 2003, *Publications of the Astronomical Society of the Pacific*, 115, 763

BIBLIOGRAPHY

- Chyży K. T., et al., 2018, *Astronomy & Astrophysics*, 619, A36
- Ciesla L., et al., 2012, *Astronomy & Astrophysics*, 543, A161
- Ciesla L., et al., 2014, *Astronomy & Astrophysics*, 565, A128
- Ciesla L., et al., 2016, *Astronomy & Astrophysics*, 585, A43
- Condon J. J., 1992, *Annual Review of Astronomy and Astrophysics*, 30, 575
- Condon J. J., Anderson M. L., Helou G., 1991, *The Astrophysical Journal*, 376, 95
- Condon J. J., Cotton W. D., Greisen E. W., Yin Q. F., Perley R. A., Taylor G. B., Broderick J. J., 1998, *The Astronomical Journal*, 115, 1693
- Cortese L., et al., 2012, *Astronomy & Astrophysics*, 544, A101
- Cortese L., et al., 2014, *Monthly Notices of the Royal Astronomical Society*, 440, 942
- For B.-Q., et al., 2018, *Monthly Notices of the Royal Astronomical Society*, 480, 2743
- Galametz M., et al., 2013, *Monthly Notices of the Royal Astronomical Society*, 431, 1956
- Giovanelli R., et al., 2005, *The Astronomical Journal*, 130, 2598
- Hao C.-N., Kennicutt R. C., Johnson B. D., Calzetti D., Dale D. A., Moustakas J., 2011, *The Astrophysical Journal*, 741, 124
- Haynes M. P., Giovanelli R., 1984, *The Astronomical Journal*, 89, 758
- Haynes M. P., et al., 2011, *The Astronomical Journal*, 142, 170
- Heald G. H., et al., 2015, *Astronomy & Astrophysics*, 582, A123
- Heesen V., et al., 2019, *Astronomy & Astrophysics*, 622, A8
- Helou G., Soifer B. T., Rowan-Robinson M., 1985, *The Astrophysical Journal*, 298, L7
- Hopkins A. M., Beacom J. F., 2006, *The Astrophysical Journal*, 651, 142
- Hughes A., Staveley-Smith L., Kim S., Wolleben M., Filipovic M., 2007, *Monthly Notices of the Royal Astronomical Society*, 382, 543
- Hurley-Walker N., et al., 2017, *Monthly Notices of the Royal Astronomical Society*, 464, 1146

BIBLIOGRAPHY

- Kapińska A. D., et al., 2017, *The Astrophysical Journal*, 838, 68
- Kauffmann G., et al., 2003, *Monthly Notices of the Royal Astronomical Society*, 346, 1055
- Kennicutt R. C., 1998, *Annual Review of Astronomy and Astrophysics*, 36, 189
- Kennicutt R. C., Evans N. J., 2012, *Annual Review of Astronomy and Astrophysics*, 50, 531
- Kennicutt R. C., et al., 2009, *Astrophysical Journal*, 703, 1672
- Kewley L. J., Dopita M. A., Sutherland R. S., Heisler C. A., Trevena J., 2001, *The Astrophysical Journal*, 556, 121
- Kroupa P., 2001, *Monthly Notices of the Royal Astronomical Society*, 322, 231
- Lequeux J., Maucherat-Joubert M., Deharveng J. M., Kunth D., 1981, *Astronomy and Astrophysics*, 103, 305L
- Madau P., Dickinson M., 2014, *Annual Review of Astronomy and Astrophysics*, 52, 415
- Martin D. C., et al., 2005, *The Astrophysical Journal*, 619, L1
- Mezger P. G., Henderson A. P., 1967, *The Astrophysical Journal*, 147, 471
- Murphy E. J., et al., 2011, *The Astrophysical Journal*, 737, 67
- Navarro J. F., Steinmetz M., 2000, *The Astrophysical Journal*, 528, 607
- Noll S., Burgarella D., Giovannoli E., Buat V., Marcillac D., Muñoz-Mateos J. C., 2009, *Astronomy & Astrophysics*, 507, 1793
- Padovani P., et al., 2017, *The Astronomy and Astrophysics Review*, 25, 2
- Peebles P. J. E., 1982, *The Astrophysical Journal*, 263, L1
- Read S. C., et al., 2018, *Monthly Notices of the Royal Astronomical Society*, 480, 5625
- Rieke G. H., et al., 2004, *The Astrophysical Journal Supplement Series*, 154, 25
- Salpeter E. E., 1955, *The Astrophysical Journal*, 121, 161
- Schawinski K., Thomas D., Sarzi M., Maraston C., Kaviraj S., Joo S.-J., Yi S. K., Silk J., 2007, *Monthly Notices of the Royal Astronomical Society*, 382, 1415

BIBLIOGRAPHY

- Schlegel D. J., Finkbeiner D. P., Davis M., 1998, *The Astrophysical Journal*, 500, 525
- Schober J., Schleicher D. R. G., Klessen R. S., 2017, *Monthly Notices of the Royal Astronomical Society*, 468, 946
- Takeuchi T. T., Buat V., Iglesias-Páramo J., Boselli A., Burgarella D., 2005, *Astronomy & Astrophysics*, 432, 423
- Taylor A. R., Stil J. M., Sunstrum C., 2009, *The Astrophysical Journal*, 702, 1230
- Tingay S. J., et al., 2013, *Journal of Physics: Conference Series*, 440, 012033
- Tinsley B. M., Danly L., 1980, *The Astrophysical Journal*, 242, 435
- Urry C. M., Padovani P., 1995, *Publications of the Astronomical Society of the Pacific*, 107, 803
- Vale A., Ostriker J. P., 2004, *Monthly Notices of the Royal Astronomical Society*, 353, 189
- Völk H., 1989, *Astronomy and Astrophysics*, 218, 67
- Wang L., Gao F., Duncan K. J., Williams W., Rowan-Robinson M., Sabater J., Shimwell T. W., 2019, *Astronomy & Astrophysics*, 109, 1
- Williams W. L., et al., 2016, *Monthly Notices of the Royal Astronomical Society*, 460, 2385
- Yun M. S., Reddy N. A., Condon J. J., 2001, *The Astrophysical Journal*, 554, 803
- de Vries W. H., Morganti R., Röttgering H. J. A., Vermeulen R., van Breugel W., Rengelink R., Jarvis M. J., 2002, *The Astronomical Journal*, 123, 1784
- van Haarlem M. P., et al., 2013, *Astronomy & Astrophysics*, 556, A2

Appendix A

Galaxy images

- A.1 Matched samples (18 samples used for the analysis)**
- A.2 Matched samples (not used for the analysis)**
- A.3 Suspicious matching samples**
- A.4 Not matching samples**

APPENDIX A. GALAXY IMAGES

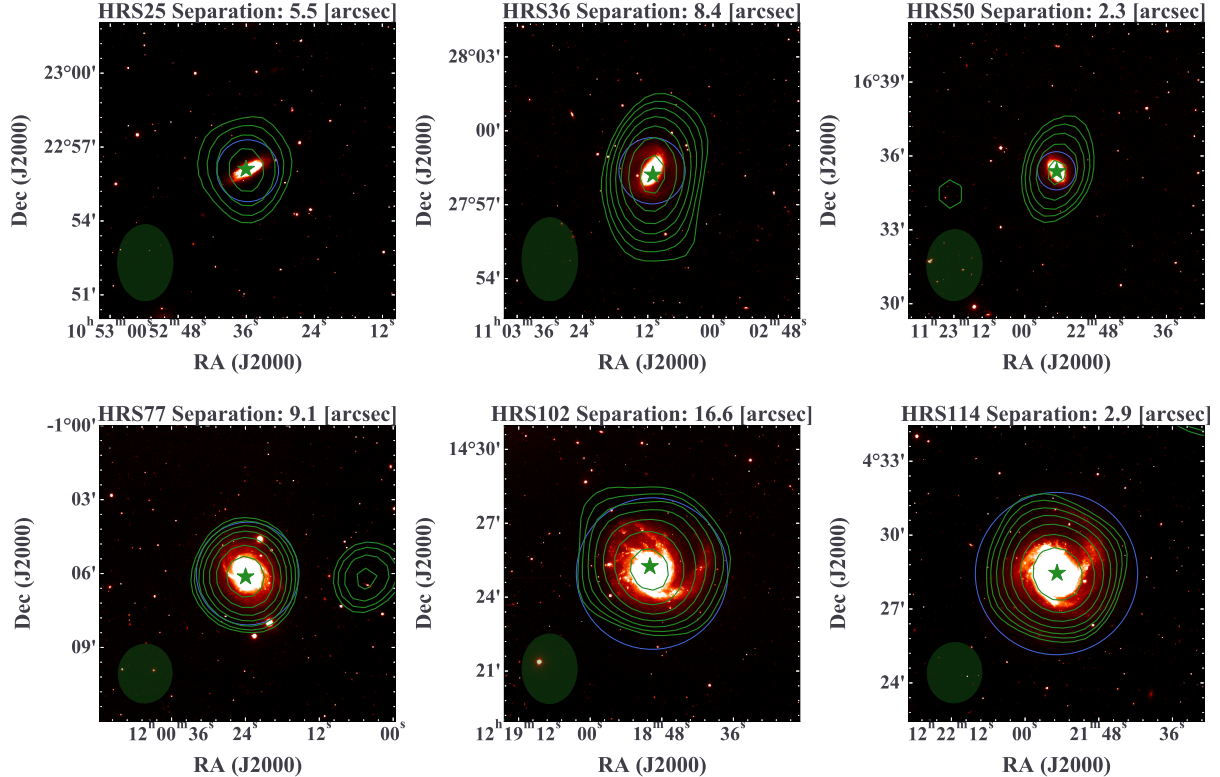


Figure A.1: These are the SDSS (Abolfathi et al. 2018) i-band images with radio contours from the GLEAM survey at 170 – 231 MHz (solid green lines). These galaxies are selected in Section 4.1 and 4.2. I draw the green contours started from the 3σ local noise and increase by a factor of the square root of 2^n (“n” is an integer). The green star marker shows the location of a radio source referred to as the GLEAM catalog. The size of this marker does not mean any feature of observations. The blue circle shows the isophotal optical size at 25 mag arcsec⁻² from Boselli et al. (2010). On the bottom left in each plot, we show the beam size of the GLEAM survey.

A.4. NOT MATCHING SAMPLES

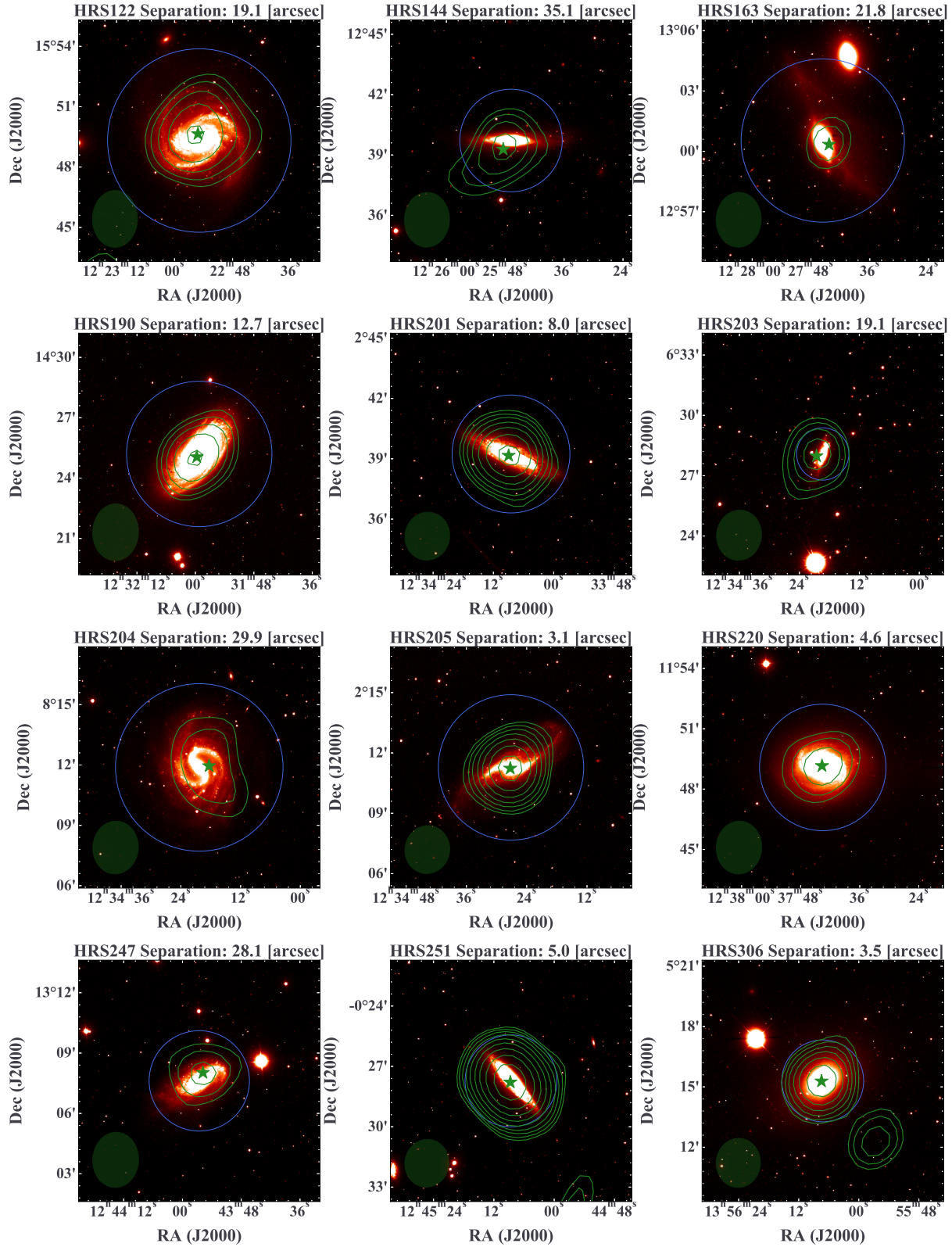


Figure A.2: Continuous.

APPENDIX A. GALAXY IMAGES

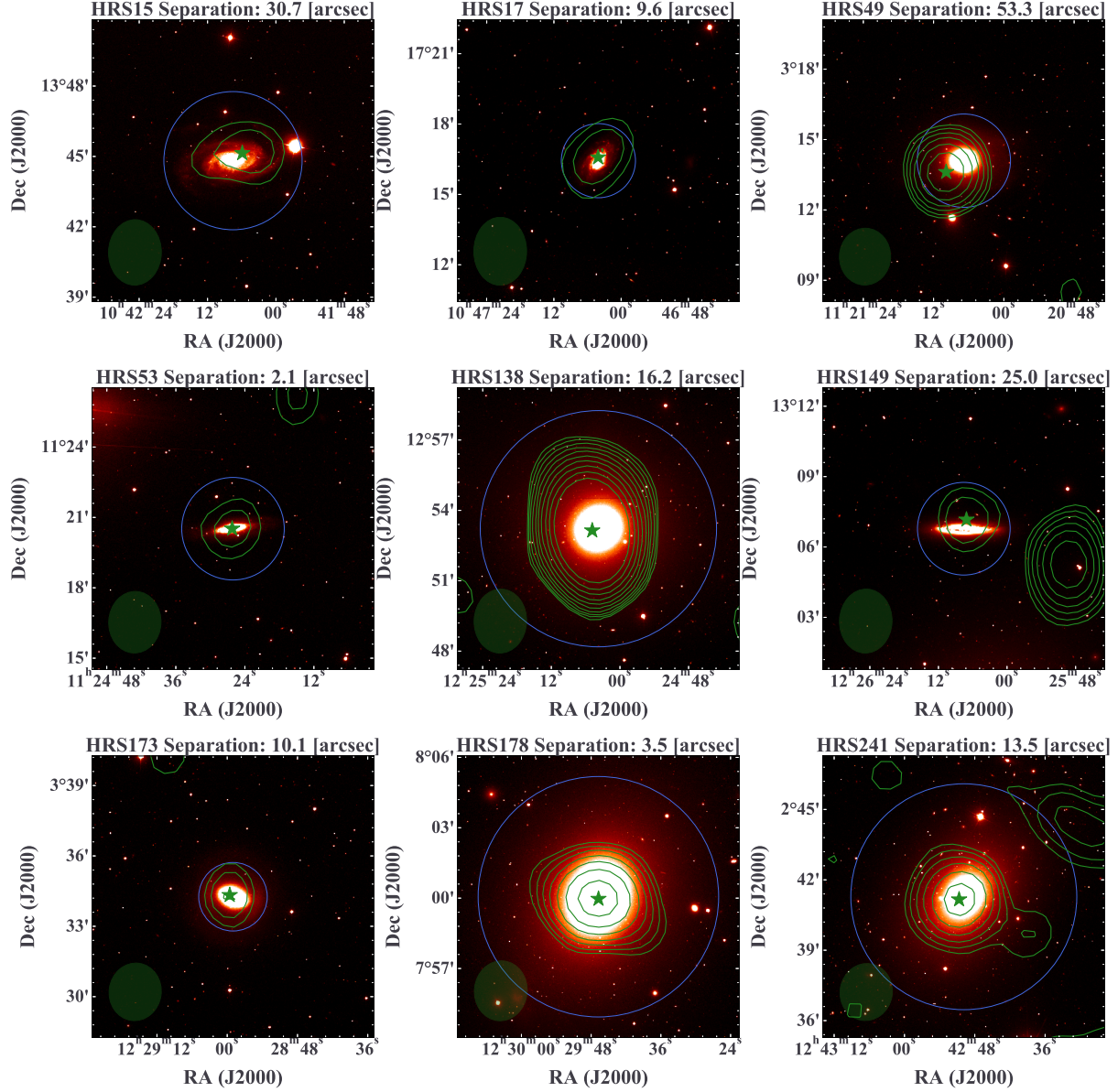


Figure A.3: These galaxies are not used for the analysis labeled in Section 4.2 although they have a radio counterpart in the GLEAM catalog by the cross-matching.

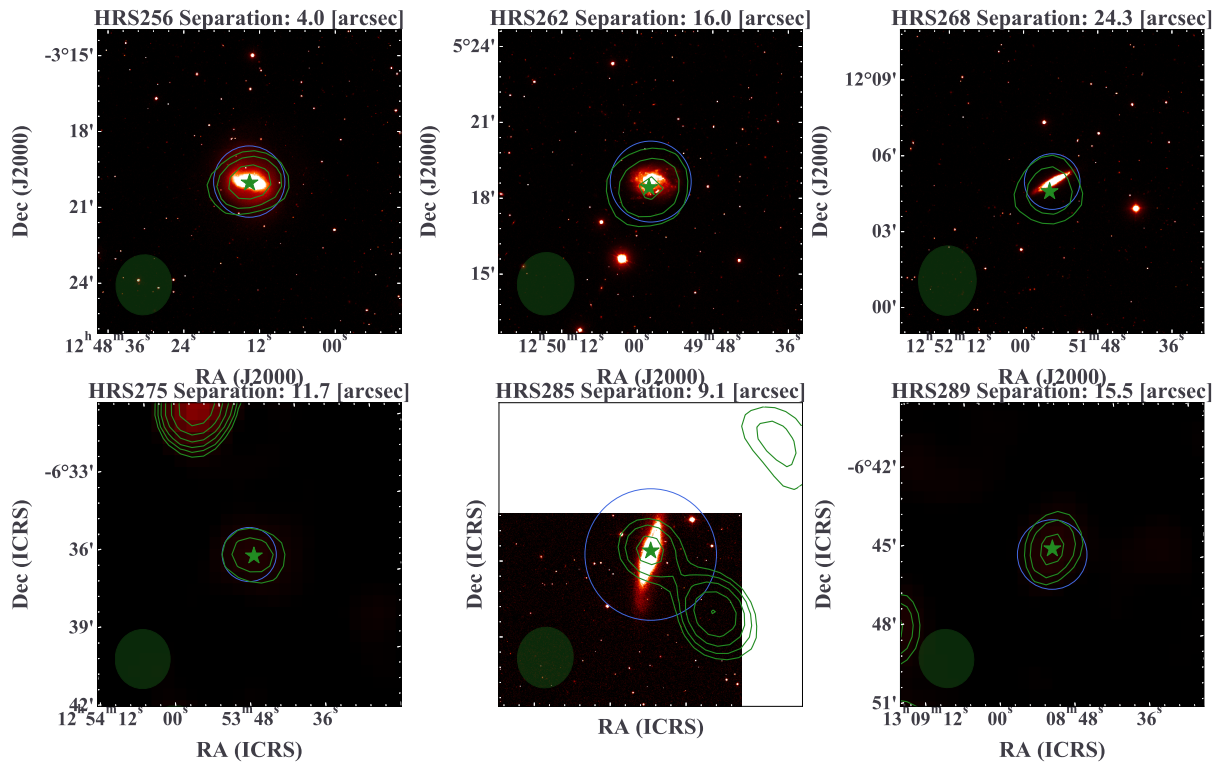


Figure A.4: Continuous.

APPENDIX A. GALAXY IMAGES

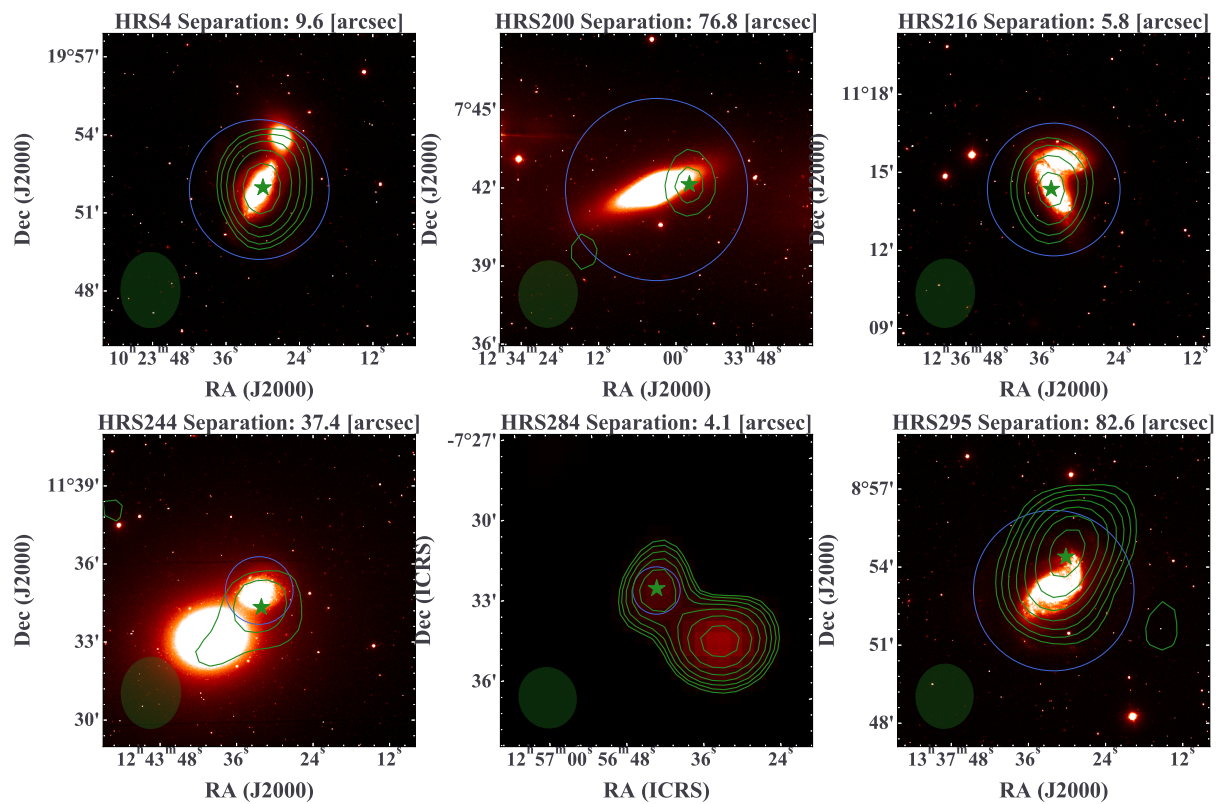


Figure A.5: These galaxies are flagged as a suspicious matching in Section 4.1

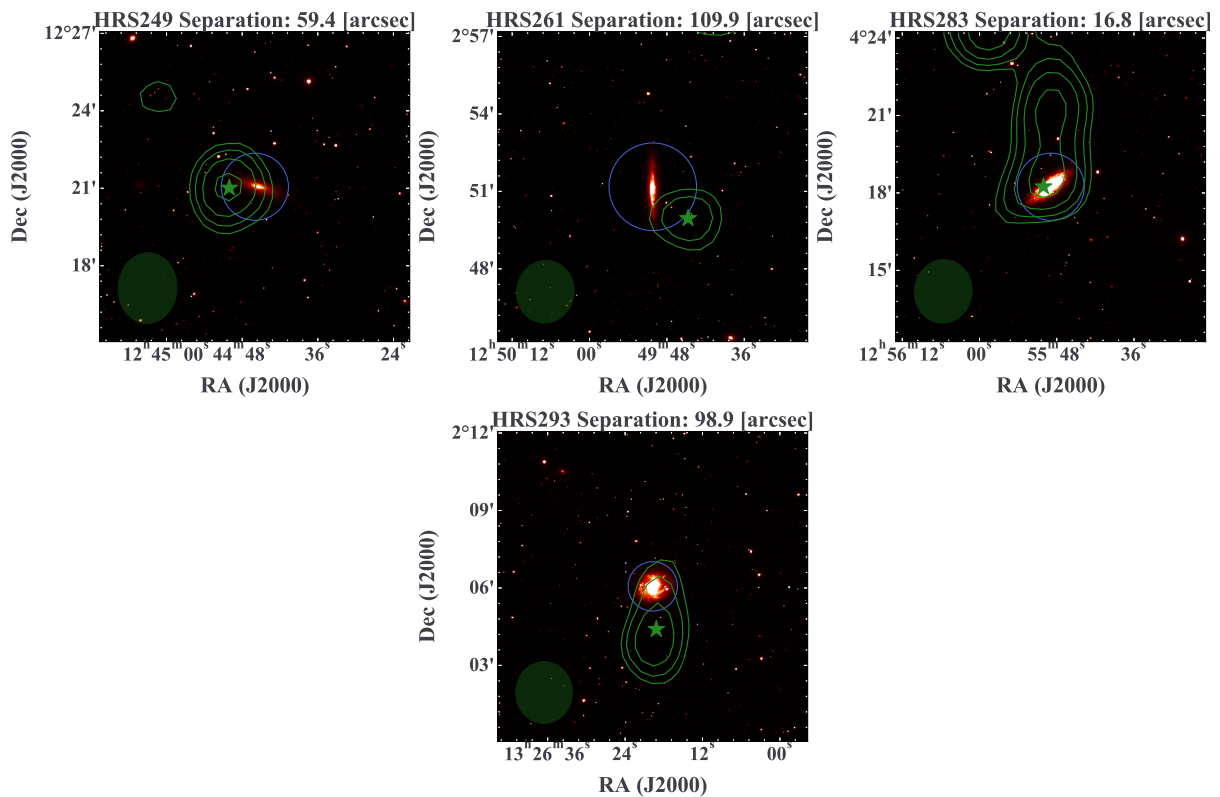


Figure A.6: These galaxies do not have a radio counterpart from the GLEAM catalog in Section 4.1

Appendix B

Galaxy samples for the analysis

APPENDIX B. GALAXY SAMPLES FOR THE ANALYSIS

Table B.1: This table shows 18 HRS galaxies selected in Section 4.1 and 4.2. Column (1) NGC (2) R.A. (3) Dec. (5) D25 (6) Dist. are from Cortese et al. (2012), column (4) Type is from Ciesla et al. (2014) (Cortese et al. 2012 for only HRS 163) and column (7) GLEAM ID refers to GLEAM catalog. γ_{MWA} , $\gamma_{\text{MWA}+1500 \text{ MHz}}$ are the result in Section 4.5. SFR_{IR} is calculated with the equation from Murphy et al. (2011) and $\text{SFR}_{\text{Radio}, 151 \text{ MHz}}$ is calculated in Section 4.6 with individual parameters. “AGN” is identified BPT diagram (e.g. Baldwin et al. 1981; Kauffmann et al. 2003; Kewley et al. 2001; Schawinski et al. 2007) with emission lines (Boselli et al. 2015). H_1 deficient galaxy is identified when the value of $\text{H}_1\text{-def}$ (Boselli et al. 2014) is larger than 0.4.

HRS	NGC	R.A.	Dec	Type	D25 [arcmin]	Dist. [Mpc]	GLEAM ID	γ_{MWA}	$\gamma_{\text{MWA}+1500 \text{ MHz}}$	SFR_{IR} [$M_{\odot} \text{ yr}^{-1}$]	$\text{SFR}_{\text{Radio}, 151 \text{ MHz}}$	AGN	$\text{H}_1\text{-def}$
25	3437	10:52:35.75	+22:56:02.9	Sc	2.51	18.24	J105236+225606	0.33+/-0.47	-0.66+/-0.07	1.41+/-0.08	0.96+/-0.28	-	-
36	3504	11:03:11.21	+27:58:21.0	Sab	2.69	21.94	J110311+275812	-0.42+/-0.1	-0.53+/-0.05	4.09+/-0.16	5.15+/-1.35	-	True
50	3655	11:22:54.62	+16:35:24.5	Sc	1.55	21.43	J112254+163522	-0.38+/-0.2	-0.63+/-0.04	1.91+/-0.07	1.45+/-0.41	-	-
77	4030	12:00:23.64	-01:06:00.0	Sbc	4.17	20.83	J120023-010607	-0.57+/-0.07	-0.63+/-0.04	4.81+/-0.19	3.55+/-0.94	-	-
102	4254	12:18:49.63	+14:24:59.4	Sc	6.15	17.00	J121850+142515	-0.7+/-0.05	-0.7+/-0.03	6.47+/-0.25	8.19+/-2.12	-	-
114	4303	12:21:54.90	+04:28:25.1	Sbc	6.59	17.00	J122154+042827	-0.57+/-0.05	-0.58+/-0.04	6.15+/-0.23	5.49+/-1.43	-	-
122	4321	12:22:54.90	+15:49:20.6	Sbc	9.12	17.00	J122255+154939	-0.77+/-0.07	-	5.45+/-0.22	4.28+/-1.14	-	True
144	4388	12:25:46.82	+12:39:43.5	Sb	5.10	17.00	J122548+123917	0.22+/-0.22	-0.73+/-0.08	1.66+/-0.06	3.09+/-0.85	Seyfert	True
163	4438	12:27:45.59	+13:00:31.8	Sb	8.12	17.00	J122744+130020	-0.81+/-0.35	-	0.69+/-0.03	2.13+/-0.66	Seyfert	True
190	4501	12:31:59.22	+14:25:13.5	Sb	7.23	17.00	J123159+142503	-0.67+/-0.12	-0.72+/-0.05	4.37+/-0.18	4.92+/-1.31	-	True
201	4527	12:34:08.50	+02:39:13.7	Sbc	5.86	17.00	J123408+023909	-0.54+/-0.06	-0.56+/-0.04	4.55+/-0.24	2.71+/-0.71	-	-
203	4532	12:34:19.33	+06:28:03.7	Im(Im/S)	2.60	17.00	J123420+062758	-0.55+/-0.13	-0.6+/-0.04	0.99+/-0.04	1.52+/-0.43	-	-
204	4535	12:34:20.31	+08:11:51.9	Sc	8.33	17.00	J123418+081157	-0.71+/-0.1	-	2.6+/-0.11	2.69+/-0.75	-	-
205	4536	12:34:27.13	+02:11:16.4	Sbc	7.23	17.00	J123427+021114	-0.61+/-0.04	-0.57+/-0.02	3.58+/-0.14	2.63+/-0.69	-	-
220	4579	12:37:43.52	+11:49:05.5	Sb	6.29	17.00	J123743+114909	-0.42+/-0.18	-0.77+/-0.05	1.56+/-0.08	2.32+/-0.65	LINER	True
247	4654	12:43:56.58	+13:07:36.0	Scd	4.99	17.00	J124355+130801	-0.27+/-0.29	-0.66+/-0.06	2.59+/-0.11	1.65+/-0.49	-	-
251	4666	12:45:08.59	-00:27:42.8	Sc	4.57	21.61	J124508-002747	-0.58+/-0.03	-0.58+/-0.02	9.2+/-0.33	9.11+/-2.35	-	-
306	5363	13:56:07.21	+05:15:17.2	pec	4.07	16.23	J135607+051516	-0.61+/-0.08	-0.51+/-0.04	0.27+/-0.03	1.75+/-0.46	-	True

Appendix C

Fitting results

APPENDIX C. FITTING RESULTS

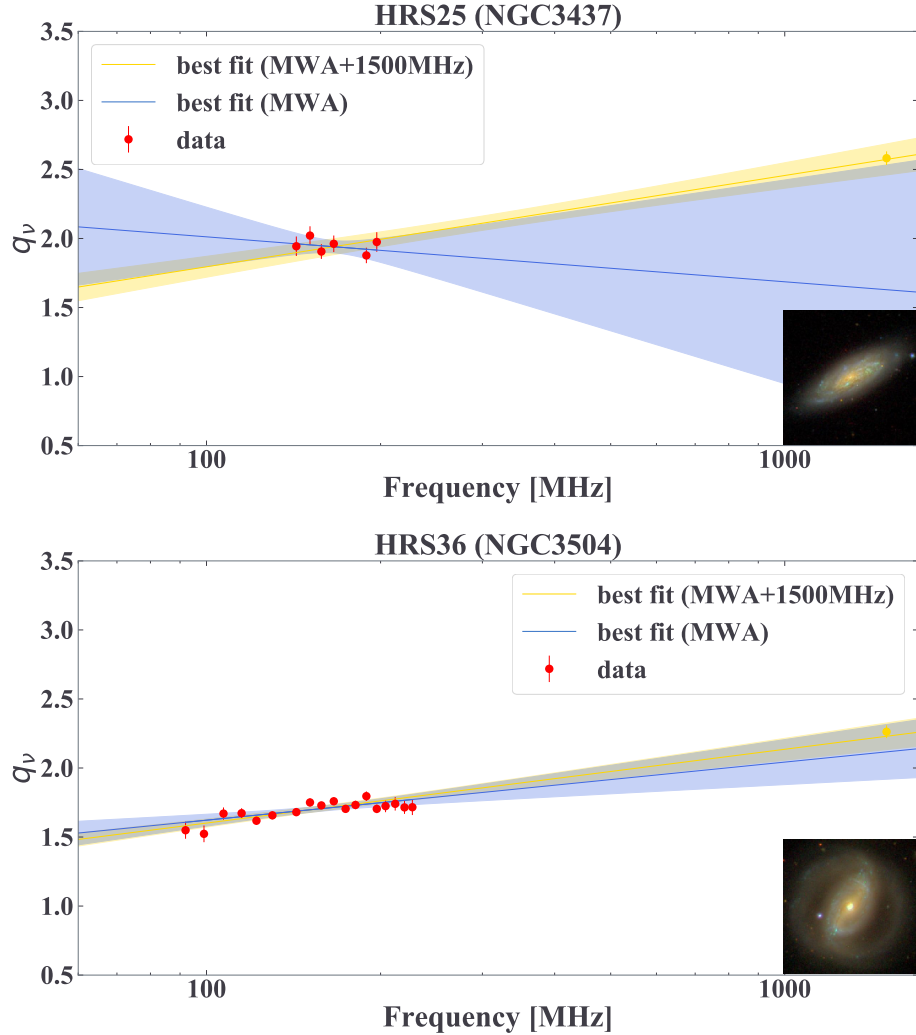


Figure C.1: These figures show the fitting result. Red points show fluxes at each MWA frequency, and a yellow point shows the flux at 1500 MHz (Boselli et al. 2015). Blue solid line shows the best fitting line, and the shaded region represents the 95% confidence interval for the fitting to MWA frequencies. Yellow line and shaded area show the fitting result with 1500 MHz besides MWA frequencies (For HRS122, 163 and 204, we do not display these because of the lack of high-quality data at 1500 MHz data). On the bottom right, we show the SDSS-RGB stacking image for each galaxy.

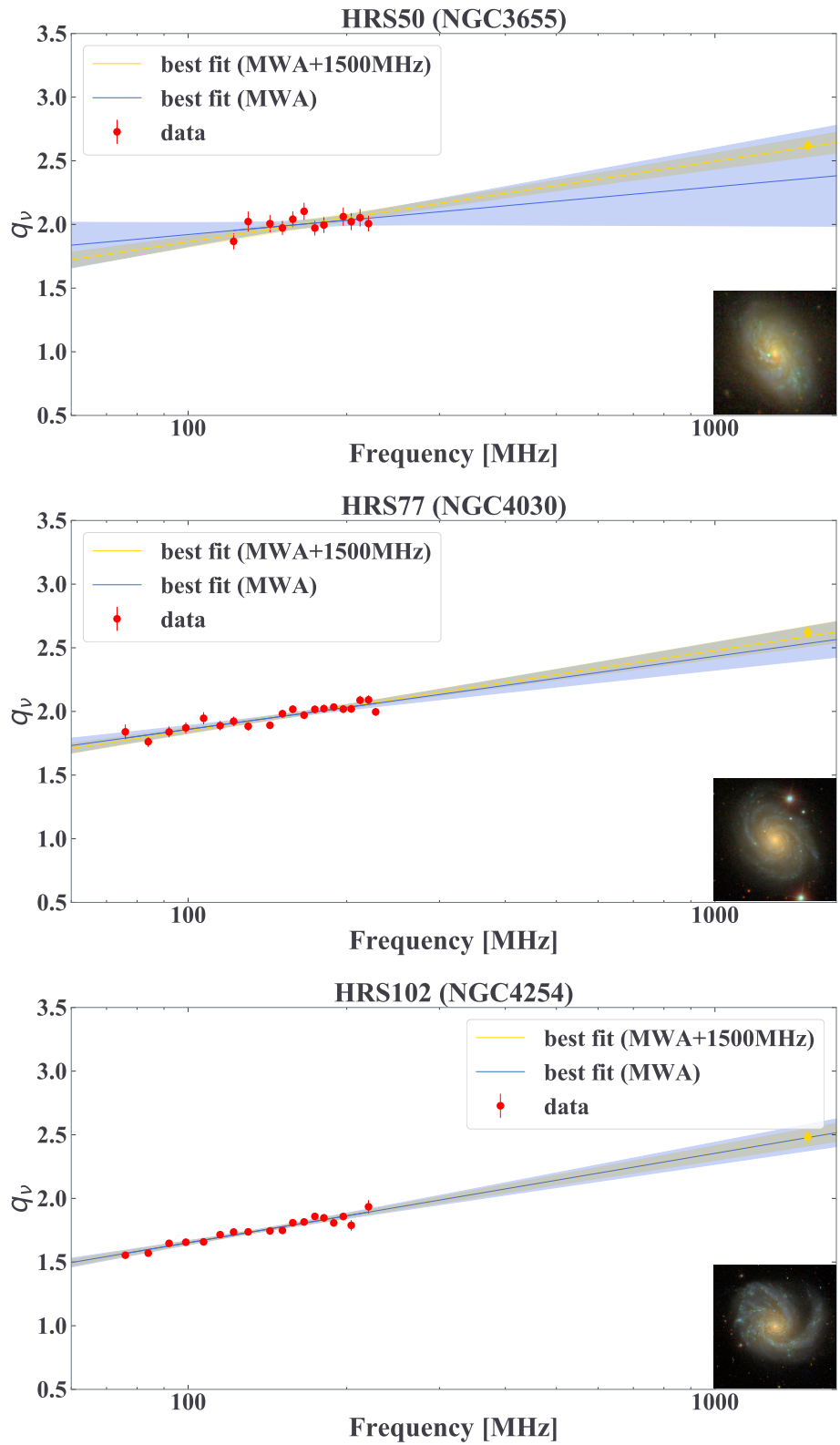


Figure C.2: Continuous.

APPENDIX C. FITTING RESULTS

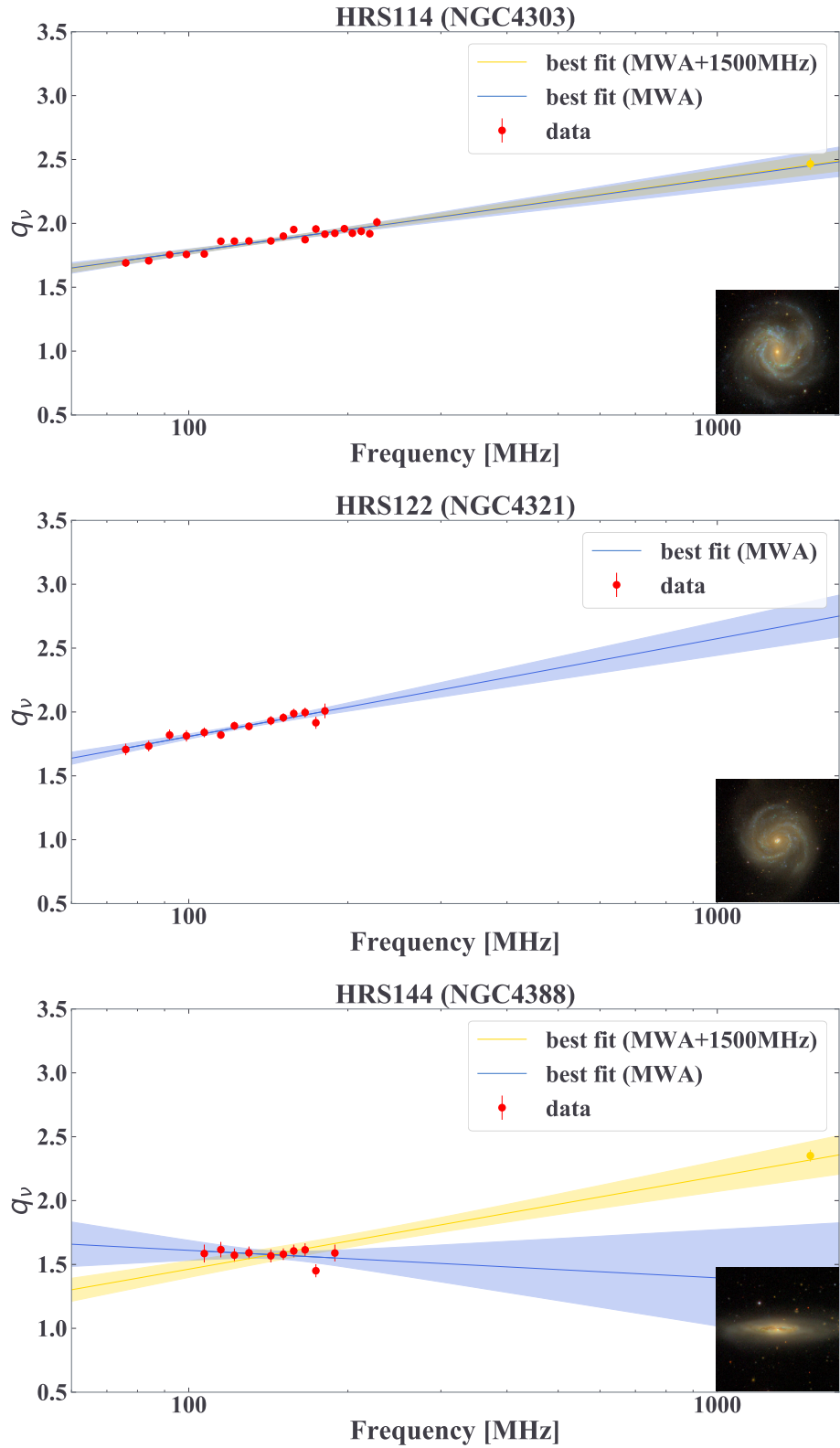


Figure C.3: Continuous.

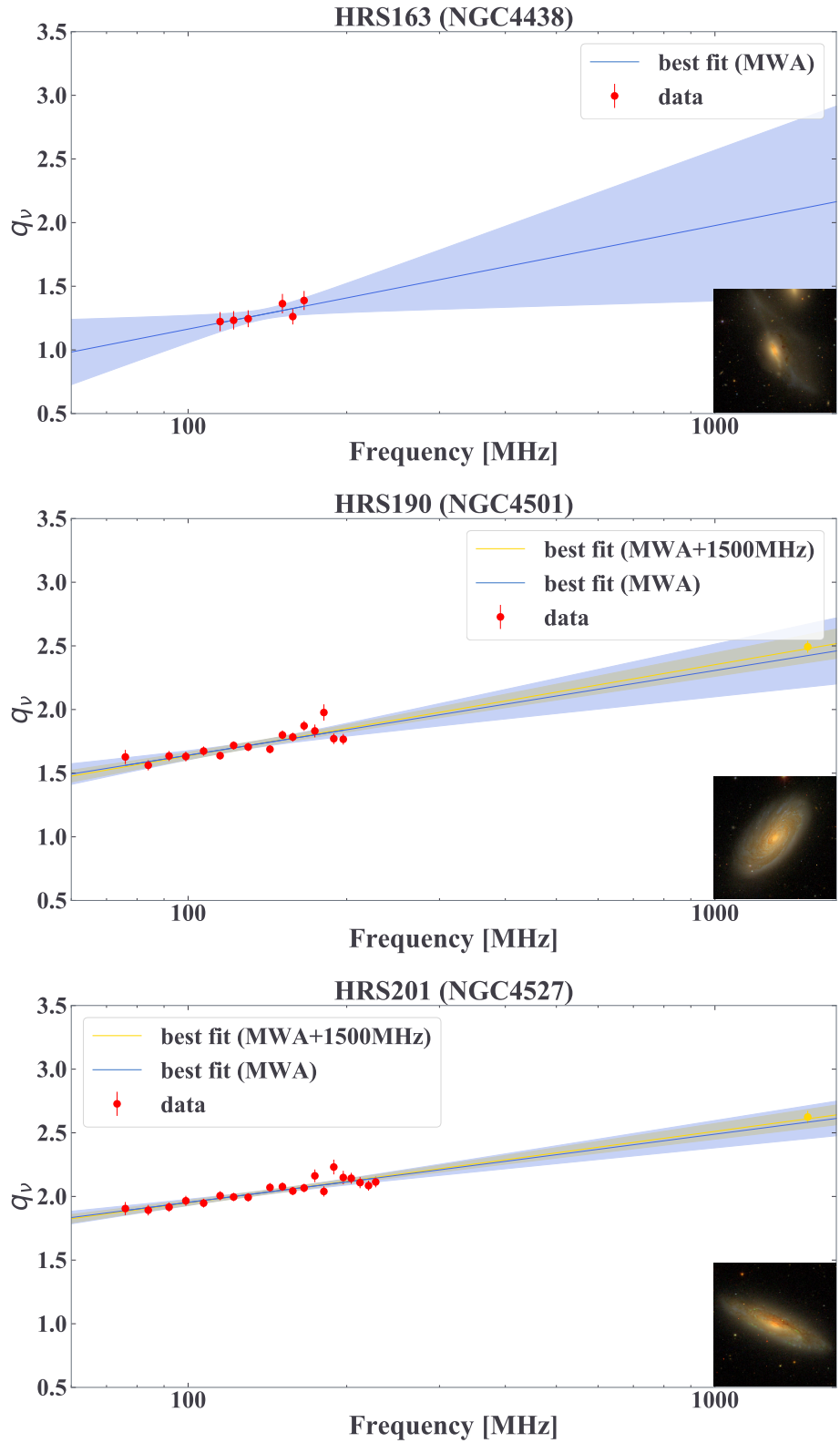


Figure C.4: Continuous.

APPENDIX C. FITTING RESULTS

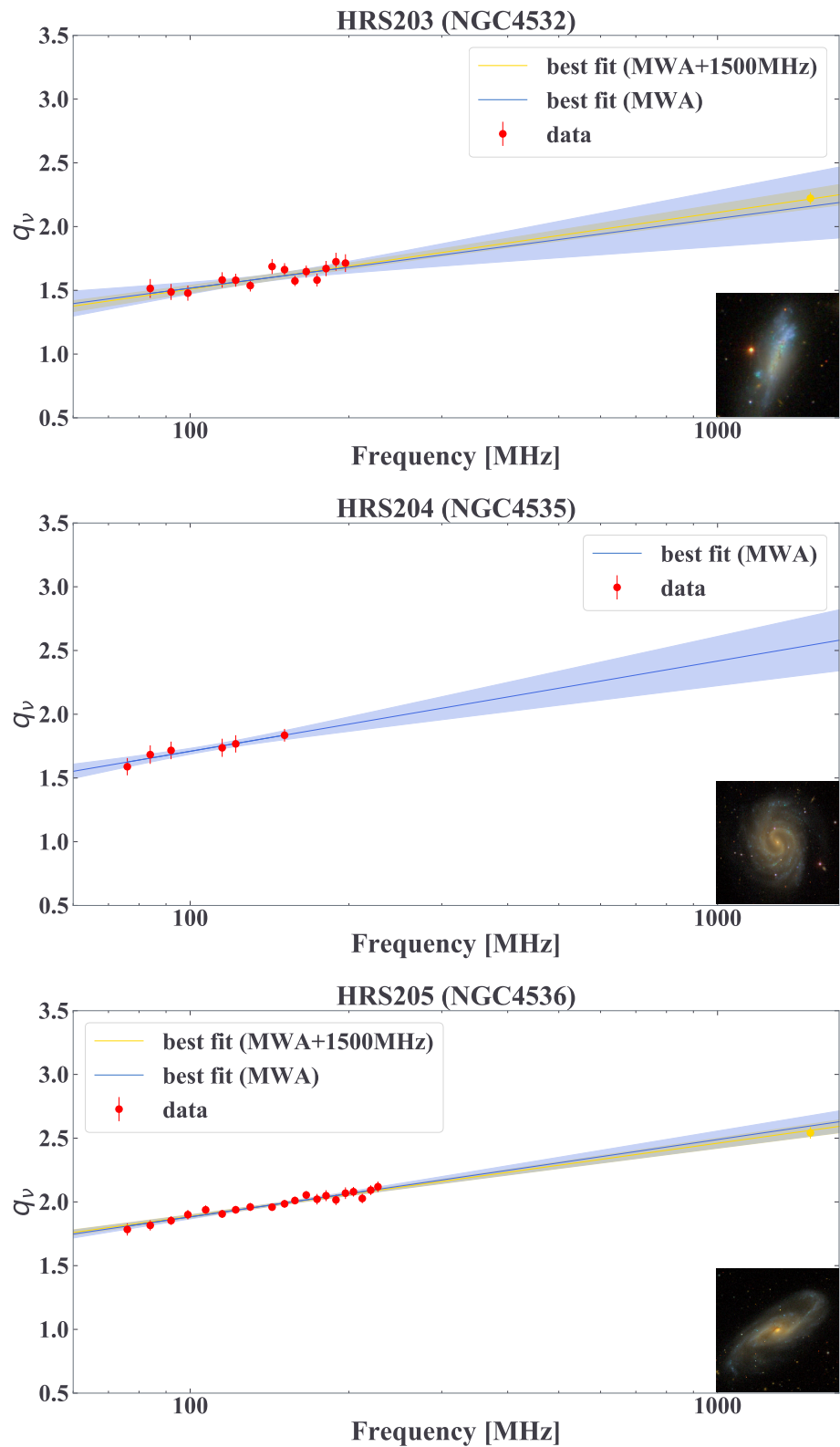


Figure C.5: Continuous.

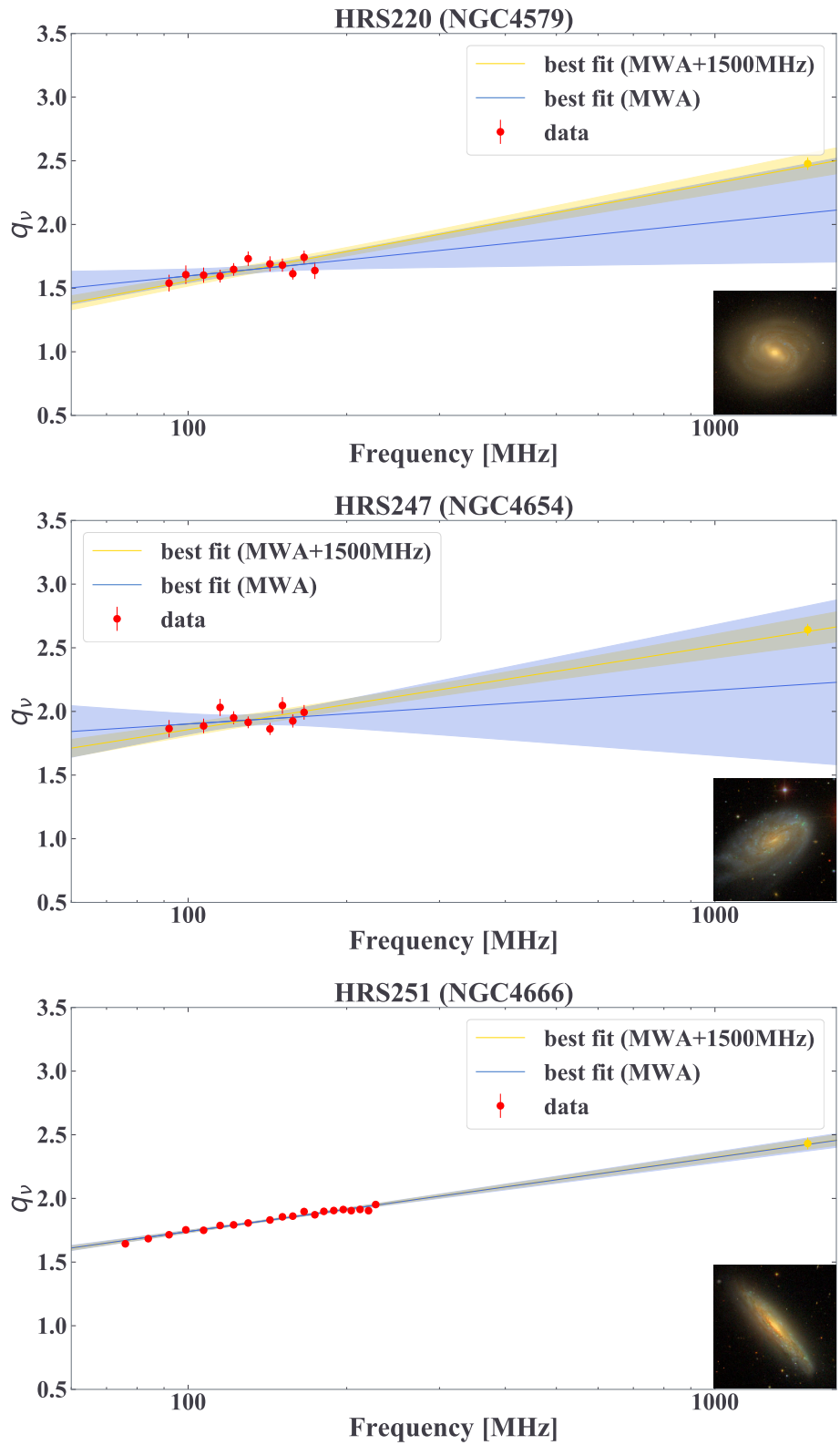


Figure C.6: Continuous.

APPENDIX C. FITTING RESULTS

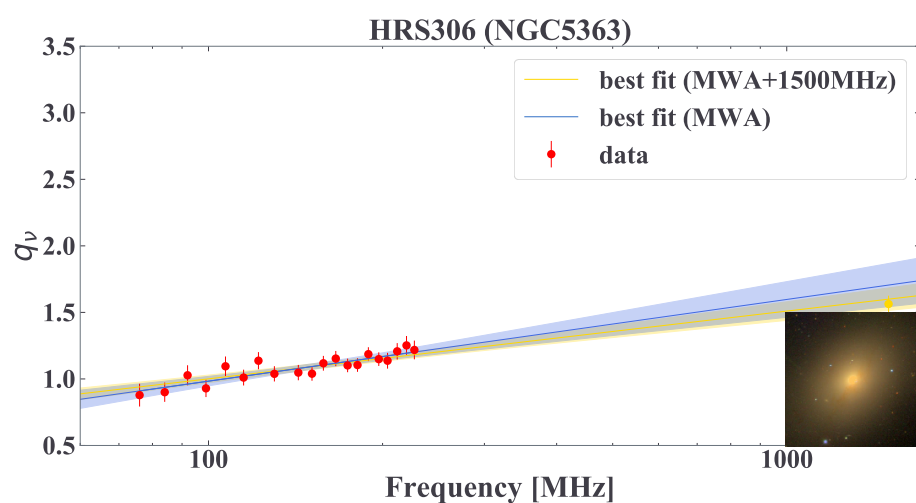


Figure C.7: Continuous.